

Controls on evolution of gas-hydrate system in the Krishna-Godavari Basin, offshore India

F. Badesab¹, P. Dewangan¹, A. Usapkar¹, M. Kocherla¹, A. Peketi¹, K. Mohite¹, S.J.Sangode² and K. Deenadayalan³

¹ CSIR - National Institute of Oceanography, Dona Paula 403004, Goa, India

² Department of Geology, Savitribai Phule Pune University, Pune-411007, India

³ Indian Institute of Geomagnetism, New Panvel, Navi Mumbai, India

Corresponding author: firoz@nio.org

Abstract

In this study, we integrate environmental magnetic, sedimentological and geochemical records of sediment core of Hole NGHP-01-10D overlying methane hydrate deposits to decipher the controls on the evolution of fracture-filled gas hydrate system in the Krishna-Godavari (K-G) basin. Four distinct sedimentary units have been identified, based on the sediment magnetic signatures. An anomalous zone of enhanced magnetic susceptibility (Unit – III: 51.9 - 160.4 mbsf) coinciding with the gas hydrate bearing intervals is due to the presence of magnetite-rich detrital minerals brought-in by the river systems as a result of higher sedimentation events in K-G basin and has no influence over hydrate formation. A strong to moderate correlation between magnetite concentration and chromium reducible sulphur (CRS) content indicates significant influence of sulfidization on the magnetic record and could be further exploited as a proxy to decipher paleo-H₂S seepage events. Analysis of high-resolution seismic, bathymetry and sub-bottom profiler data reveals the existence of a regional fault system in K-G basin. The opening and closing dynamics of the faults facilitated the migration and trapping of required gas concentrations resulting in accumulation of gas hydrates at the studied site. The seismic data provides support to the rock-magnetic interpretations. The observed variations in magnetic and geochemical properties have resulted from the episodic flow of methane and sulphide-enriched fluids through the fracture-filled network formed as a result of shale-tectonism. Our study demonstrated the potential of using an enviro-magnetic approach in combination with other proxies to constrain the evolution of gas hydrate system in marine environments.

1. Introduction

Methane hydrate is the most common and natural form of gas hydrates, and is distributed worldwide along the oceanic and permafrost environments [Kvenvolden, 1993]. In marine settings, the studies on gas hydrate system are focussed on addressing a variety of scientific investigations like estimation of energy resource, impact on climate change, and ocean acidification and assessment of submarine slope stability [Kvenvolden, 1993; Milkov, 2004; Boswell and Collett, 2011]. The genesis and occurrence of methane hydrate are controlled by many factors such as pressure-temperature conditions, availability of methane or other lighter hydrocarbon gases, migration pathways of fluid, sediment provenance and trapping efficiencies of host sediments and neo-tectonic activity [Kvenvolden et al., 1993; Wu and Ruppel, 1999; Mazurenko et al., 2003; Hesse, 2003; Haacke, et al., 2008; Simonetti et al., 2013]. Therefore, a multi-disciplinary investigation is required to understand the influence of sediment provenance, shale-tectonism, diagenesis and authigenesis on the evolution of the gas hydrate system.

Reductive diagenesis is a common process in sulfide-rich marine sedimentary environments where anaerobic sulfate reduction and bacterially mediated degradation of organic carbon produce hydrogen sulfide (H₂S). Further, the iron-bearing minerals react with the available H₂S to produce magnetic iron sulfides which have distinct magnetic signatures [Karlin and Levi, 1985; Dewangan et al., 2013; Roberts, 2015]. At cold seep-environments large amounts of hydrogen sulfide are produced as a result of anaerobic oxidation of methane. The geochemical processes associated with formation and dissociation of methane hydrates may cause precipitation of secondary (diagenetic) minerals which can be easily detected using environmental magnetic methods [Housen and Musgrave, 1996; Horng and Roberts, 2006; Fu et al., 2008; Estban et al., 2008]. Therefore, magnetic characterization of detrital and diagenetic mineral phases in a gas hydrate environment could provide clues to the geochemical processes associated with gas hydrate formation, migration and dissociation.

Drilling and coring activities on board JOIDES Resolution during the national gas hydrate drilling expedition (NGHP-01) confirmed the occurrence of fracture-filled gas hydrates at several sites in the continental slope of the K-G basin [Kumar et al., 2014]. Geophysical studies showed high spatial variability in distribution of gas hydrate concentrations as it is primarily controlled by a large fault system [Dewangan et al., 2011]. One of the drilled sites NGHP-01-10D showed a ~ 128 m thick layer of gas hydrates and the overall gas hydrate saturation estimated was in the order of 25 - 30 %

[*Lee and Collett, 2009*]. The analysis of seismic and well-log data showed the occurrence of a fracture-filled gas hydrate system at the studied site [*Collett et al., 2008*]. The evidence of paleo-methane seepages are observed in the vicinity of NGHP-01-10D [*Mazumdar et al., 2009*]. Further, the magnetic studies by *Dewangan et al.* [2013] reported the diagenetic alteration of magnetic minerals in a short sediment core (~ 30 m: MD161/8). In the present study, we attempt to establish the linkage between gas hydrates and associated magnetic signals in K-G offshore basin by investigating a 198 m long sediment core (NGHP-01-10D) from a proven gas hydrate / cold seep environment of K-G basin. The magnetic data is studied in combination with seismic, geochemical and sedimentological proxies to understand the evolution of fracture-filled gas hydrate system in K-G Basin.

2. Geology of Krishna-Godavari Basin

The Krishna-Godavari basin (K-G basin) is a proven petroliferous basin located in the central part of the eastern continental margin of India (ECMI) (Figure 1). The basin covers an area of about 28,000 km² onshore and 145,000 km² offshore (*Rao, 2001*). The ECMI evolved during the break-up of eastern Gondwana landmass around 130 Ma ago when India separated from East Antarctica [*Ramana et al., 2001*]. The basin receives a huge supply of detrital sediments through Krishna and Godavari river systems. The Holocene-Pleistocene deposit of the K-G basin is dominated by smectite bearing Godavari clay formations [*Rao, 2001*]. A sediment thickness of 3–5 km in the onshore and about 8 km in the offshore region has been reported [*Bastia, 2007; Prabhakar and Zutshi, 1993*]. The annual sediment transport of the Krishna and Godavari rivers is estimated to be 67.7 and 170×10^6 metric ton, respectively [*Biksham and Subramanian, 1988; Ramesh and Subramanian, 1988*].

The gas hydrate deposit in K-G basin is established from geological and geophysical studies. The seismic data showed occurrences of Bottom Simulating Reflector (BSR) in K-G basin related to gas hydrate. Further, the drilling and sediment coring activities onboard DV JOIDES Resolution confirmed the presence of gas hydrates in K-G basin [*Collett et al., 2008, Dewangan et al., 2010, Shankar and Riedel, 2010*]. Various geomorphic structures such as mounds, shale diapirs and faults are formed due to ongoing neo-tectonics in the K-G basin. The bathymetric mounds are mostly associated with fluid/gas migration occurring through the fault system, and favour the accumulation of gas hydrates in K-G basin [*Dewangan et al., 2010*].

3. Methodology

3.1. Magnetic measurements

A 198.4 m long sediment core NGHP-01-10D was collected onboard DV JOIDES Resolution from K-G basin (Figure 1). The entire sediment core was sub-sampled at intervals of 1.5 m to 6 m following IODP standards. All magnetic measurements were made on dry sediment samples packed in 1-inch cylindrical sample bottles at the paleomagnetic laboratory of CSIR-National Institute of Oceanography (NIO). Magnetic susceptibility measurements were performed using the Bartington MS2B dual frequency susceptibility meter. Susceptibility was measured at two different frequencies $\chi_{lf} = 0.47$ kHz and $\chi_{hf} = 4.7$ kHz. The frequency dependent susceptibility was computed as $\chi_{fd} \% = (\chi_{lf} - \chi_{hf}) / \chi_{lf} \times 100$. Anhyseric remanent magnetisation (ARM) was imparted using 100 mT AF field superimposed with a fixed DC bias field of 50 μ T and measured using a Molspin Minispin spinner magnetometer. Susceptibility of ARM is calculated as mass normalized ARM divided by the DC bias field. Isothermal remanent magnetisation (IRM) of 1 T in the forward direction and -20 mT, -30 mT, -100 mT and -300 mT in the backward direction were imparted to the sediment samples using MMP10 pulse magnetizer and measured using Molspin Minispin spinner magnetometer. Mass-normalized IRM acquired with a peak field of 1T is assumed to be the saturation isothermal remanent magnetization (SIRM). S-ratio is computed as the ratio between the IRM at -300 mT and IRM at 1 T (IRM_{-300mT} / IRM_{1T}) [Thompson and Oldfield, 1986].

The specific measurements were carried out at Indian Institute of Geomagnetism, Panvel, India. Temperature dependence of magnetic susceptibility ($\chi-T$) was measured in a field of 300 A/m at 875 Hz by a CS-3 furnace unit coupled to an Agico (KLY-4S) Kappabridge. The high temperature measurements were performed from room temperature to 700°C in argon atmosphere. The hysteresis loop analyses were performed using Princeton measurements of the micromag 2900 series alternating gradient magnetometer (AGM) in field cycling between ± 1 T.

3.2. Physical properties and grain size analysis

After splitting the sediment cores, the samples were taken from the working half, and the sediment bulk, grain densities and porosity were measured using a penta-pycnometer following IODP protocols. This data is available through NGHP Expedition - 01 initial report. The sediment grain size analyses were carried out on Malvern Mastersizer 2000 Laser Particle Size Analyzer at CSIR - NIO. Prior to analysis, the sediment samples were desalinated and subsequently decarbonated using

dilute HCl (1 N). Organic carbon was removed by 10% H₂O₂. Na-hexametaphosphate was added to the final suspension to ensure dispersion throughout the analysis. The grain size values are reported as volume %.

3.3. Magnetic mineral extraction, SEM-EDS and XRD analysis

The magnetic minerals were extracted from the bulk sediment following the procedure of *Petersen et al.* [1986]. A scanning electron microscope (JEOL JSM-5800 LV) was used to capture images of the magnetic grains in secondary electron (SE) imaging mode at energy levels between 15 and 20 kV. The elemental analysis was performed using an energy dispersive X-ray spectroscopy (EDS) probe attached to the microscope. The identification of magnetic mineralogy of selected samples from different depth intervals of the NGHP-01-10D core was carried out using a Rigaku X-Ray Diffractometer (Ultima IV). The samples were run from 15° to 70° 2θ at 1°/min scan speed using Cu Kα radiation ($\lambda = 1.5414 \text{ \AA}$).

3.4. Geochemical analysis

The sulfur isotope ratios of Chromium reducible sulfur ($\delta^{34}\text{S}_{\text{CRS}}$), CRS and TOC data for the NGHP-01-10D core are taken from *Peketi et al.* [2012]. More details on extraction method of CRS and elemental sulfur can be found at *Peketi et al.* [2012].

4. Results

4.1. Rock-magnetic and geochemical properties of Hole NGHP- 01-10D

Four distinct units (I-IV) are demarcated based on down-core variation in magnetic properties in core NGHP-01-10D (Figure 2). The unit - I (1.4 - 12.8 mbsf) shows the reduction in magnetic susceptibility. A down-core decrease in magnetic susceptibility and SIRM (Figures 2a and 2b) values suggests the decrease in concentration of magnetic minerals in this unit. A substantial decrease in S-ratio is observed at 8.2 mbsf (Figure 2c). The increase in χ_{fd} (%) values in unit-I and unit-II indicates fining in magnetite crystal size (Figure. 2d). A trend of down-core increase in CRS and TOC content is observed (Figures 2e and 2g). The beginning of unit - II (13.6 - 45.7 mbsf) is marked by a sharp decrease in magnetic mineral concentration as reflected by χ and SIRM (Figures 2a and 2b). An increase in χ_{fd} (%) followed by low magnetic susceptibility indicates higher abundance of magnetically weak fine-grained minerals in this unit (Figures 2a and 2d). A pronounced increase in

CRS content is observed throughout in this unit. The TOC content varies from 1.2 to 2.1 wt % and CRS content varies between 0.16 to 1.74 wt% in this unit (Figures 2e and 2g). The $\delta^{34}\text{S}_{\text{CRS}}$ also increases in this unit, and two peaks of $\delta^{34}\text{S}_{\text{CRS}}$ enrichment as well as enhancement of Mo are observed at 22.5 mbsf and 43.7 mbsf suggesting H₂S seepage events [Peketi *et al.*, 2012] (Figure 2f).

The beginning of unit - III (52.0 - 160.4 mbsf) is marked by an increase in magnetic mineral concentration (χ , SIRM) (Figures 2a -2b). The magnetic susceptibility increases by an order of magnitude as compared to that of unit I and unit-II. The S-ratio is close to unity throughout this unit, but shows a region of lower S-ratio between 109.1 and 122.3 mbsf indicating the presence of higher coercivity magnetic minerals (Figure 2c). The lower end of this unit (160.4 mbsf) is marked by a decrease in susceptibility, SIRM, S-ratio and approximately matches the depth of BSR at this site [Kumar *et al.*, 2014]. Two distinct patterns in the variation of TOC content are observed. Initially, TOC decreases from 45.7 mbsf to 94.0 mbsf and later increases downcore from 96.1 mbsf to 151.4 mbsf (Figure 2g). Three peaks of episodic enrichment in $\delta^{34}\text{S}_{\text{CRS}}$ are observed at 94.0 mbsf, 113.5 mbsf and 160.4 mbsf, respectively (Figure 2f) [Peketi *et al.*, 2012].

The unit - IV (180.0 - 198.4 mbsf), below the present BSR depth, is marked by a sudden drop in magnetic mineral concentration as indicated by low χ and SIRM (Figures 2a and 2b). The low χ_{fd} (%) suggest the dominance of coarse magnetic grains in this unit (Figure 2d).

4.2. Magnetic hysteresis curves and temperature-dependent magnetic susceptibility

The day plot shows that majority of the samples lie in the pseudo-single domain (PSD) [Day *et al.*, 1977] (Figure 3a). Housen and Musgrave, [1996] defined the magnetic grain size index D_{JH} as the ratio of two axes in the Day plot i.e., $\{J_{\text{rs}} / J_{\text{s}}\} / \{H_{\text{cr}} / H_{\text{c}}\}$. The ratios are used to examine the magnetic grain size in gas hydrate bearing sediments. The D_{JH} values vary between 0.052 and 0.079 (Figure 3b). The highest values of D_{JH} were observed within the gas hydrate zone (Unit- III) of Hole-NGHP-01-10D, indicating the dominance of coarse magnetic grains in this zone. A drop in D_{JH} value in unit- II reflects the dominance of fine grained magnetic minerals (Figure 3b).

Figures 4a-4d show the representative curves of temperature dependent magnetic susceptibility for samples from units- I, II, III and IV. In all analyzed samples, a major decrease in susceptibility at high temperatures (above 550 °c) indicates that the magnetic mineralogy is dominated by titanomagnetite (Figures 4a-4d). The small increase in magnetic susceptibility with increasing temperature, i.e., above 400 °c, can be attributed to the presence of pyrite in these units (Figures 4a-4d).

4.3. Grain size distributions and physical properties of host sediments

Silt and clay constitute the bulk sediment grain size fractions at site NGHP-01-10D (Figure 5). The silt and clay content ranges from 14.56 - 52.29 vol % and 47.62 - 83.56 vol%, respectively. The sand content is lower and varies from 0.016 - 7.37 vol %. Few layers of relatively higher sand concentrations are observed throughout the core. These fine sand layers are also marked by low susceptibility indicating the presence of magnetically weak, coarse grains in these intervals (Figure 5).

The properties of host sediments affect the formation and distribution of gas hydrates. Therefore, the bulk properties of core NGHP-01-10D are presented along with the magnetic susceptibility (Figure 6). The bulk density varies from 1.37 to 1.77 with an average of 1.67 g /cm³, and the grain density varies from 2.53 to 2.79 g /cm³ with an average of 2.72 g /cm³ (Figures 6a and 6b). The bulk and grain densities show opposite trend in Unit - I, but follow a similar trend of down-core increase in unit -II and unit - III (Figures 6a and 6b). A large drop in grain density is observed around 128.0 mbsf (Figure 6b). The porosity profile mirrors the bulk density profile (Figure 6c). The higher susceptibilities were found associated with grains possessing higher bulk and grain density especially in unit-III (Figure 6d).

4.4. Electron microscopy and energy dispersive spectra (EDS) analysis on magnetic separates

The electron microscopic images and EDS spectra of mineral extracts from different sedimentary units are shown in Figure 7 and Figure 8. Several ferri-magnetic iron oxides and sulphide-rich particles of various sizes and shapes are identified (Figure 7 and Figure 8). In unit - I, the mousy and etching features on titano-magnetite grain provide evidence of dissolution of magnetic minerals in this unit (Figures 7a and 7b). The EDS results of the titano-magnetite grains from unit I show the presence of titanium and iron with traces of manganese, vanadium, silicon, calcium, potassium and phosphorus (Figures 7a and 7b). Large aggregates of cubic pyrite crystals that have overgrown framboids are observed in the zone of low magnetic susceptibility of unit - II (Figures 7c and 7d and Figure 2a). The EDS results of magnetic grain from unit II show the presence of iron and sulfur with minor amounts of vanadium, silicon, potassium, calcium and germanium (Figure 7c). In unit - III, most of the extracted magnetic mineral grains appear to be well preserved but mild reductive dissolution is observed (Figures 8a -8f). The EDS results from unit III show the presence of iron, titanium, sulfur and phosphorous with traces of manganese, vanadium, silicon, calcium, potassium and germanium (Figures 8a - 8e). A skeletal type, most probably titano-hematite grain, with

quadrangle plate-like structure is also observed in this unit at 151.4 mbsf (Figure 8d). In Unit - IV, the presence of numerous titano-magnetite grains with overgrowths of pyrite framboids are noticed (Figures 8g and 8h). The EDS results from unit IV show the presence of sulfur with trace amount of iron and titanium suggesting the presence of pyrite in this sample (Figure 8g, spectra-2).

4.5. Identification of magnetic minerals using X-ray diffraction analysis

The X-ray diffraction curves of magnetic minerals from different sedimentary units are shown in Figure 9. The titano-magnetite is the dominant magnetic mineral found in all sedimentary units in varying proportions (Figures 9a-9d). The XRD peaks in the regions (unit-II and unit-IV) of reduced magnetic susceptibility confirm the presence of pyrite (Figures 9b and 9d). A small peak corresponding to pyrite is also observed in unit – III (Figure. 9c).

4.6. The relationship between magnetic, sedimentological and geochemical parameters

Bivariate data plots are used to examine the relationships between magnetic, sedimentological and geochemical parameters (Figures 10a-10d and Figures 11a-11f). A positive correlation between magnetic susceptibility and SIRM is observed in all the samples, but with different slopes indicating the presence of ferri- and para-magnetic mineral assemblages in the samples (Figure 10a). A clear relationship between magnetic susceptibility (χ_{ir}) and magnetic grain size indicators ($\chi_{fd}\%$) is observed with highest values of susceptibility being dominated by coarser magnetic grains from the unit - III (Figure 10b). It is interesting to note that a trend of fining in magnetic grain size is seen in unit-I, II and IV, where finer grains showed higher magnetic susceptibility (Figure 10b). Overall, for most of the samples, S-ratio varies between 0.82 and 1 and show a wide range in $\chi_{fd}\%$ values indicating the abundance of mixed grain size mineral assemblages in the studied samples. The lower s-ratio in samples from unit-III reflects minor presence of hard coercive minerals in this zone (Figure 10C).

A strong correlation is observed between CRS content and magnetic susceptibility for unit- I ($R^2=0.797$) and moderate correlation for unit-III ($R^2=0.3293$). Weak or no correlation is observed for unit- II ($R^2=0.064$) and unit- IV ($R^2=0.1023$) (Figure 10d). A trend of decrease in susceptibility with increasing CRS content is clearly visible in unit-I and unit-III, whereas samples from unit- II and unit-IV possessed much lower and uniform susceptibilities, but showed a wide range in CRS content (Figure 10d). This correlation provides clues on the marked influence of H₂S seepages (sulfidization)

on mineral magnetic record and this relationship needs to be tested further to be used as a proxy to decipher the paleo-H₂S seepage events.

In general, based on the magnetic mineral record of the entire core two major zones can be identified (Figures 10a-10c). Zone -1 (diagenetically modified): Samples from unit-I, II and IV possess low susceptibility, SIRM, S-ratio > 0.82 and show fining in magnetic grain sizes as indicated by wide range in χ_{fd} % values. Zone - 2 (Non-diagenetic): samples from unit III possess high susceptibility and SIRM, low χ_{fd} % suggesting the presence of detrital, diagenetically unaltered magnetic grains (Figures 10a-10c). Recent study by *Dewangan et al.*, [2013] showed that the higher χ_{fd} (%) values (> 10) suggest the occurrence of super-paramagnetic (SP) sized ferri-magnetic minerals possibly due to the presence of greigite. In our samples, the presence of significant amounts of greigite is unlikely due to low χ_{fd} % together with negative observations in SEM imagery (Figure 2d, Figures 7a-7d, Figures 8a-8h and Figures 10a-10d).

The good covariation between magnetic susceptibility and silt content suggests that the highest concentration of magnetic minerals is within the silt fraction (Figure 11b). A reverse trend of decrease in magnetic susceptibility with increase in sand and clay content is observed (Figures 11a and 11c). The cross plot between grain size parameters and CRS content shows that highest enrichment of sulfur occurs within clay fraction compared to sand and silt content (Figures 11d-11f).

5. Discussion

The rock-magnetic, geochemical and sedimentological investigations of the sediment core NGHP-01-10D showed four distinct sedimentary units which may be controlled by the combined interaction of sediment provenance (detrital), transport pathways and post-depositional processes (diagenesis, authigenesis). Since the presence of gas hydrate is established in core NGHP-01-10D, we attempt to relate these sedimentary units to the occurrence of gas hydrates with an aim to understand the evolution of the gas hydrate system in K-G basin.

5.1. Detrital inputs and magnetic susceptibility variations in K-G basin

The higher values of magnetic susceptibility, SIRM and lower χ_{fd} (%) in unit- III can be directly attributed to the coarse-grained detrital Fe-Ti rich grains which were supplied by Krishna and Godavari river system to the basin as a result of high energy driven sediment transport event [*Ramprasad et al.*, 2011] (Figures 2a, 2b and 2d, Figure 4c, Figures 8a-8f and Figure 9c). We

hypothesize that unit- III represents the period of intense sediment (detrital) supply event which might have led to rapid burial and preservation of these detrital material forming a magnetic-rich layer in deeper sediment strata in the K-G basin. The electron microscopy in combination with EDS and XRD analysis on the magnetic extracts confirms the presence of unaltered coarse magnetic grains with well-preserved morphology primarily of detrital origin which supports our hypothesis (Figures 8a-8f and Figure 9c).

In marine sediments, the sedimentation rate plays an important role in controlling early diagenesis of magnetic minerals in addition to other factors including supplies of organic matter, availability of sulfate and reactive iron [Berner, 1984; Canfield, 1991]. As sedimentation increases, the contact time between reactive iron and available sulphidic-rich fluids decreases which leads to hindering of early diagenetic processes and preservation of detrital mineral grains [Reidinger *et al.*, 2005]. Furthermore, we have made an attempt to examine the influence of higher sedimentation events on the early diagenetic processes in K-G basin. The decrease in magnetic susceptibility in unit-II and unit-IV could be attributed directly to reductive dissolution and pyritization of magnetic minerals taking place in these units (Figure 2a). These units are characterized by lower values of susceptibility, SIRM indicating low concentration of magnetic minerals. The XRD and SEM-EDS analysis of magnetic grains confirms the presence of pyrite in these units (Figures 7c and 7d, Figures 8g and 8h, Figures 9b and 9d).

Studies by Ramprasad *et al.*, [2011] provided evidences of the occurrence of MTD's and high sedimentation rate events in K-G basin. The MTD's are inferred based on seismic signatures from high resolution sparker data, multibeam bathymetry, ¹⁴C age-depth curve and physical properties data. They further proposed that the presence of steep topographic gradients, high sedimentation rates and a regional fault system might have facilitated the sediment slumping/sliding in the K-G basin. The higher values of magnetic susceptibility in unit-III suggest good preservation of magnetic minerals which may be attributed to such high sedimentation rate events. High sedimentation rate leads to rapid burial of detrital magnetic minerals and thus less affected by early diagenesis. One plausible hypothesis that explains the sudden drop in magnetic susceptibility at 159.5 mbsf is the lower sedimentation rate in unit IV. It is highly possible that lower sedimentation rate could have enhanced the pyritization in unit-IV prior to the commencement of unit-III. The occurrence of pyrite and partially altered titanomagnetite grains in unit-IV support the hypothesis (Figures 8g and 8h and Figure 9d).

5.2. Influence of sediment composition on development of gas hydrate system in K-G basin

In addition to well-established controls including temperature, pressure and salinity, the sediment composition profoundly influences the formation, distribution and morphology of gas hydrates. Previous studies showed that the gas hydrate growth is enhanced in sand and coarse grained sediments which provides conducive environment for hydrate nucleation [Soloviev and Ginsburg, 1997; Clennell et al., 1999; Ginsburg et al., 2000; Torres et al., 2008; Kars and Kodama, 2015]

The sediment grain size measurements were made on the representative samples from hydrate bearing as well as non-hydrate bearing intervals of the core NGHP-01-10D to examine the influence of sediment porosity on hydrate formation processes. At the studied site, unit-III represents a zone where highest gas hydrate concentrations were found. The higher silt and clay concentrations and relatively low sand content in this unit suggests that the sediment grain size is not a vital factor controlling the hydrate formation (Figure 5 and Figure 6c). Recent studies have reported the occurrence of pore -filling hydrates in fine grained matrix from the volcanic ash of the Andaman Sea in the Bay of Bengal [Winters, 2011] and in coarse grained sediments at Blake Ridge [Lorenson, 2000]. These findings suggest that the hydrate nucleation can even take place in mixed-grained (fine and coarse) sediments if significantly higher methane concentrations and favourable P-T are available.

The sediment bulk and grain density are important factors controlling the permeability of the host sediments which play a major role in local trapping of gas and providing the fluid flow to the hydrate reservoirs. In Unit III, we observed a minor increase in bulk and grain densities (Figures 5a and 5b). Teichert et al. [2014] identified several layers of non-evenly distributed hard authigenic carbonates which were preferentially buried as a result of higher sedimentation and remain constrained as specific horizons throughout the core. In unit- III, the observed increase in bulk and grain densities and relatively low sediment porosity could be directly attributed to the occurrence of authigenic carbonates (Figures 6a-6c). Therefore, the increase in bulk and grain densities may not have significant influence on the formation of gas hydrate in this unit.

At site NGHP-01-10D, the gas hydrate stability zone coincides well with the anomalous zone of higher magnetic susceptibility in unit- III. Next question to be answered was whether there is any linkage between higher magnetic susceptibilities exhibited by these Fe-Ti rich mineral layers and hydrate occurrences (Figure 2a, Figures 8a-8f and Figure 9c). Larrasoana et al., [2007] observed higher magnetic susceptibility in gas hydrate bearing zones at Southern Hydrate ridge, Cascadia

Margin. They identified authigenic greigite and pyrrhotite minerals which were formed as a byproduct of microbially-mediated diagenetic reactions in these zones. The good correlation between magnetic susceptibility and silt content suggest that highest magnetite concentrations occurs within the silt-size fraction which in-turn offered relatively lower porosity compared to sand (Figure 11b). This suggests that the abrupt increase in magnetic susceptibility in this unit is only due to the occurrence of silt-sized magnetite rich (PSD) particles which were brought in by the Krishna and Godavari river system as a result of past higher sedimentation events and were deposited in the basin (Figures 8a-8f, Figure 3a). Therefore, we conclude that there is no linkage between the association of higher magnetic mineral concentrations and the formation of hydrates.

The bulk sediment mineralogy is another factor which may influence the hydrate nucleation and has been successfully used to characterize and exploit gas hydrate reservoirs [Egawa *et al.*, 2015]. Overall, the sediment bulk magnetic mineralogy of the studied core is dominated by primary ferri-magnetic Fe-Ti rich magnetic grains with a few diagenetically precipitated pyrite occurrences in unit-II and unit-IV (Figures 2a-2c, Figures 4a-4d, Figures 7a-7d, Figures 8a-8h and Figures 9a-9d). A recent mineralogical study on sediments from a gas hydrate reservoir at the East Nankai highlighted the significance of using the bulk sediment mineralogy to gain more insights into the geo-mechanical behaviour and permeability of the gas hydrate reservoir [Egawa *et al.*, 2015]. In our studied core, although we observe variations in sand, silt and clay content, the bulk sediment mineralogy remains uniform as confirmed from magnetic, mineralogical and electron microscopic data (Figures 2a-2c, Figures 4a-4d, Figure 5, Figures 7a-7d, Figures 8a-8h and Figures 9a-9d). The above observations suggest that the sediment mineralogy has no significant influence over hydrate formation in K-G basin. Further, we try to investigate the possible source of magnetic minerals in the K-G basin. Previous studies demonstrated that Krishna and Godavari rivers are the main drainage systems passing through the source rocks of the Krishna-Godavari basin sediments which are derived from the Late Cretaceous Deccan basalt sources and late Archaean-early Proterozoic peninsular gneissic complexes [Ramesh and Subramanian, 1988; Sangode *et al.*, 2007]. In our studied samples, the rock-magnetic mineralogy diagnostic parameter (S-ratio), temperature dependent magnetic susceptibility curves and XRD, SEM-EDS analyses on magnetic grains indicated that the sediments are mostly dominated by relatively higher concentration of ferri-magnetic Fe-Ti rich grains mainly sourced from proximal Deccan basalts with minor amounts of titanohematite / goethite (Figure 2c, Figures 4a-4d, Figures 7a-7d, Figures 8a-8h and Figures 9a-9d).

5.3. Linkages between neo-tectonic events and gas hydrate dynamics in K-G basin

The tectonic history of the region is another significant factor influencing the formation of methane hydrates. The development of fault system induced by tectonic activities has been shown in K-G basin [Dewangan *et al.*, 2010; Shankar and Riedel, 2010; Mazumdar *et al.*, 2009, Choudhori *et al.*, 2011]. The downward movement of sediment mass over highly pressurized shale strata drives the shale tectonics [Damuth, 1994; Wu and Baily, 2000]. This movement of over pressured strata creates faults, folds and upthrusting of the over burden strata resulting in the development of bathymetric mounds and ridges [Dewangan *et al.*, 2010]. Such structures act as conduits for migration pathways for gas through the sediment strata and accumulation of gas over longer periods resulting in accumulation of methane hydrates if suitable P-T conditions are present.

The depth migrated seismic section in the vicinity of NGHP-01-10D is shown in Figure 12a and the interpreted depth section is shown in Figure 12b. The details of seismic data processing and velocity model building are discussed by Dewangan *et al.* [2011] and Jaiswal *et al.* [2012a, 2012b]. The occurrence of subsurface gas hydrate is manifested in the seismic data by the presence of well-demarcated BSR. Some of the major horizons like the gas bearing layer and Layers L1-L4 are interpreted in the seismic section. Five major fault systems (F1-F5) have been reported in the vicinity of the studied core [Dewangan *et al.*, 2011] out of which three major faults F1, F3 and F4 are highlighted in the section Figure 12b. A pronounced discontinuity is observed in all the interpreted horizons in the vicinity of faults F1 and F3. Further, the movement along the fault systems has resulted in the formation of a seafloor mound. In order to access the timing of the activation of the fault, the throw of the fault across the interpreted horizons is calculated and shown in Figure 12c. Interestingly, the throws of the fault across F1 (~ 50 m) and F3 (~35) are almost constant for all the horizons. The negative sign of the throw indicates that the depth of the horizon decreases with increasing CDP number and vice versa. The constant throw of the fault indicates sudden movement of all the horizons along the fault rather than a creep which involves a steady, gradual movement along the faults. The faults appear to be later than the deposition of layer L4 as the earlier layers (L1-L3) are affected by the faults. The coastal side of the mound is filled by recent mass transport deposits (MTDs) which onlap onto the layer L4 as well as the fault F1. We interpret that the major fault systems (F1-F5) got activated at the base of unit II. Recent studies by Riedel *et al.*, [2010] and Mandal *et al.*, [2014] showed that the area surrounding the site NGHP-01-10D is dominated by a series of MTD's or debris flows. High resolution seismic data suggests that the occurrence depth of recent MTD is around 16 mbsf. Previous studies identified the presence of buried paleo-

chemosynthetic community and concretions of authigenic carbonates at this depth [Mazumdar *et al.*, 2009; Collett *et al.*, 2008, Teichert *et al.*, 2014, Kocherla *et al.*, 2015]. We hypothesize that the seepage of methane gas from the exposed faults led to the proliferation of chemosynthetic communities, formation of thick authigenic carbonates with high magnesium content [Mazumdar *et al.*, 2009; Teichert *et al.*, 2014; Kocherla *et al.*, 2015] and led to the dissolution of detrital magnetic minerals due to H₂S released as a result of anaerobic oxidation of methane [Dewangan *et al.*, 2013]. At the same time, gas hydrates might have been accumulated in the hydrate stability zone (unit III). The formation of gas hydrate along the fault system eventually leads to the closure of the faults as gas hydrates act as impermeable deposits. We believe that the deactivation of the fault system occurs at the top of unit II. The present day deposits (unit I) do not show any signatures of methane seepage, or the formation of near-surface authigenic carbonates. Therefore, we hypothesize that the major fault systems (F1-F5) must have been activated at the base of unit II and got closed at the top of unit-II (Figure 13).

5.4. Sediment diagenesis, migration of paleo-sulfate methane transition zone (SMTZ) and precipitation of authigenic and biogenic minerals.

Sediment diagenesis is one of the important post-depositional factors influencing the magnetic record of the sediment core. During diagenesis, the detrital iron minerals react with available H₂S generated as a result of bacterial activity via-/through sulfate reduction processes occurring during the decomposition of organic matter and anaerobic oxidation of methane (AOM) [Berner, 1970]. At site NGHP-01-10D, the sulfate -methane transition zone lies between 15-16 mbsf [Kumar *et al.*, 2014] (Figure 2). The decrease in magnetic susceptibility in unit- I followed by a sharp drop in susceptibility in unit- II provides evidence for dissolution of iron oxides and precipitation of ferri-magnetic iron sulphides in this unit (Figure 2a, Figures 7c and 7d and Figure 9b). The lower magnetic susceptibility in unit - II indicates that intense pyritization took place in this zone [Dewangan *et al.*, 2013]. The SEM-EDS, temperature-dependent susceptibility and mineralogical data provide evidences of the occurrences of pyrite and titano-magnetite in this unit (Figures 4a-4d, Figures 7c and 7d, and Figure 9b).

Studies by Clennell *et al.*, [1999] reported that diagenesis occurs when the sediments are frozen into solid hydrate cement. In our core, most of the gas hydrates are concentrated in unit - III (51.9 to 160.4 mbsf). Although the bulk mineralogy of the sediments within this unit is dominated by ferri-magnetic titano-magnetite grains, we observed sharp drops in magnetic susceptibility at different

intervals (61.02 mbsf, 79.5 mbsf, 93.97 mbsf, 103.5 mbsf, 109.1mbsf, 121.22 mbsf, 130.53 mbsf) (Figure 5). The signature of diagenesis at these depths is observed in optical microscopy which shows a thin layer of orange-reddish coloured pyrite coatings on many of the magnetic grains (data not shown). The enrichment of CRS is also observed at some of these depths (94.0 mbsf, 113.5 mbsf and 160.4 mbsf) suggesting that the enhancement of pyritization leads to reduced susceptibility in both Unit II and III. It is likely that the decrease in sedimentation during these periods might have increased the contact time between iron minerals and available reactive sulphide-rich fluids enhancing the pyritization process [Canfield and Berner, 1987] or the intensification of AOM. A broad zone of lower S-ratio is observed between 110.3 mbsf and 122.3 mbsf which corresponds to lower susceptibility. The drop in S-ratio is due to the preservation of higher coercivity minerals at these intervals which was further confirmed by electron microscopy data (Figures 2a, and 2c and Figure 8d). The survival and preservation of these minerals from diagenetic processes could be best explained by the fact that the titanohematite offers more resistance to the early and late diagenetically induced geochemical attack and they are less prone to reductive dissolution [Channel and Hawthorne, 1990; Yamazaki et al., 2003; Cornell and Schwertmann., 2003; Liu et al., 2004; Poulton et al., 2004; Nowaczyk, 2011].

In an anoxic sedimentary environment, the location of sulphate methane transition (SMT) boundary is controlled by AOM and the depth of SMT boundary depends on the methane fluxes i.e., higher methane fluxes result in shallow SMT depths and vice versa [Borowski et al., 1996; Knittel and Boetius, 2009]. The production of CRS in marine sediments is controlled by available reactive iron (diagenetic product) and the concentration of hydrogen sulfide [Neumann et al., 2005]. Studies by Peketi et al. [2012] demonstrated that the sulfate reduction processes fuelled by AOM at SMT boundary is imprinted in the isotopes of CRS ($\delta^{34}\text{S}_{\text{CRS}}$) and, therefore, can be used along with enhanced Molybdenum (Mo) concentrations to decipher the present and paleo-SMT boundaries. In the studied core of NGHP-01-10D, Peketi et al., [2012] identified five zones of enriched $\delta^{34}\text{S}_{\text{CRS}}$ throughout the core (22.5 mbsf, 43.7 mbsf, 94.0 mbsf, 113.5 mbsf, 160.4 mbsf) that are suggestive of paleo H_2S seepages due to episodic methane expulsions in K-G basin (Figure 2f). The cross-plot between CRS and susceptibility in Unit III suggests that the increase in CRS leads to decrease in susceptibility (Figure 10d) confirming that the drop in susceptibility is due to enhanced pyritization. The occurrence of several bands of authigenic carbonates (AGC) through the core at site NGHP-01-10D indicates that the episodic intensification of AOM at a different times (depth/age) led to the precipitation of such carbonates layers [Teichert et al., 2014]. The highly depleted carbon isotopic

composition of these carbonates is indicative of a methane-derived source [Teichert *et al.*, 2014]. Recent studies have also shown that the paleo-depth of SMT controls the reductive dissolution of Fe-oxides and precipitation of Fe-sulfides leading to marked decrease in magnetic susceptibility and such transformation of magnetic minerals due to enhanced AOM activity have been well documented [Kasten *et al.*, 1998; Jorgensen *et al.*, 2004; Riedinger *et al.*, 2005; Novosel *et al.*, 2005; Hornig and Chen, 2006]. The AOM process causes enhanced enrichment of hydrogen sulfide and bicarbonates which triggers precipitation of iron sulphides at SMT leading to distinct magnetic signatures [Jorgensen *et al.*, 2004; Ussler and Paull, 2008].

Biogenic magnetic minerals produced by magnetotactic bacteria are ubiquitously found in sedimentary environments and have important implications in paleomagnetic and environmental magnetic studies [Kirschvink and Chang, 1984; Petersen *et al.*, 1986; Stolz *et al.*, 1986; Hounslow and Maher, 1996; Roberts *et al.*, 2012; Heslop *et al.*, 2013]. These fine -grained magnetites can be easily detected using specific rock-magnetic and electron microscopic (SEM, TEM) techniques [Petersen *et al.*, 1986; Vali *et al.*, 1987; Chang *et al.*, 2012]. The SEM-EDS observations and magnetic hysteresis measurement made on magnetic extracts from different sediment depth intervals suggest that the magnetic particles are dominated by titanomagnetites (PSD) with few occurrences of pyrite (Figure 3a, Figures 7a-7d and Figures 8a-8h). We were unable to detect any signature of biogenic magnetic minerals in the studied samples.

5.5. Can magnetic record be used as a potential tracer to identify the fossil gas hydrate zone in the K-G basin?

In marine settings, the dissociation of gas hydrates takes place whenever P-T condition changes as a result of tectonic related activities or climate change. The development of fault system induced by shale tectonic activity or submarine landslides could alter the pressure and temperature conditions [Sloan, 1998]. One can speculate that, whenever the suitable P-T conditions prevail, hydrate nucleation takes place leaving the former boundary of gas hydrate stability zone (GHSZ) as a fossil gas hydrate horizon. In K-G basin, the present base of GHSZ calculated using hydrate stability equation is ~ 150 mbsf [Dewangan *et al.*, 2010; Shankar and Riedel, 2010]. Studies by Joshi *et al.* [2014] reported the methane release events caused by gas hydrate destabilization at the studied site based on the carbon stable isotopic analysis of planktic and benthic foraminifera. The geological and geochemical processes associated with gas hydrate formation and dissociation has a measurable magnetic signature. At Hydrate Ridge on Cascadia margin, Musgrave *et al.* [2006] reported that the

microbial activity in the presence of gas hydrates leads to the formation of iron sulfides. They observed that the base of GHSZ is marked by an abrupt reduction in magnetic grain size indicative parameter (D_{IH}) which is defined as the ratio of J_{rs} / J_s and H_{cr} / H_c in the Day plot. Similarly, *Housen and Musgrave* [1996] noticed a sharp decrease in (D_{IH}) below the GHSZ at sites 889 and 890 off Vancouver Island and site 892 off Oregon coast and suggested that once the hydrate dissociates the SD greigite, which was earlier formed in the gas hydrate zone got transformed into pyrite in the free gas zone i.e below BSR and therefore these zones can be marked as fossil gas hydrate intervals.

In our studied sediment core NGHP-01-10D, the interval of unit - IV i.e below BSR (160.4 - 198.5 mbsf) shows a sharp decrease in magnetic susceptibility, an abundance of pyrite grains and the relative increase in CRS concentration at 160.4 mbsf (Figures 2a and 2f and Figures 8g-8h). It is interesting to note that the top of unit-IV coincides with the base of the gas hydrate stability zone (GHSZ) suggesting that the magnetic values in unit-IV is likely to be governed by deep diagenetic processes rather than early diagenetic or depositional processes. Similar occurrence of lower magnetic values below the GHSZ is also observed for the Site NGHP-01-05 suggesting the possibility of deep pyritization processes in K-G basin [*Kumar et al.*, 2014]. The seismic data suggests the presence of deeper gas bearing horizon below the BSR [*Dewangan et al.*, 2011]. The velocity model also suggests the presence of free gas below the BSR [*Jaiswal et al.*, 2012a,b]; however, the presence of only methane gas in unit IV cannot explain the observed dissolution / depletion of Fe-oxides. The presence of both methane and sulphate/H₂S is required for deep pyritization processes. The next question is what could be the possible sources of the sulphate/H₂S availability at this depth. The findings by *Housen and Musgrave* [1996] suggest that the H₂S which is required to complete the pyritization process sometimes gets trapped and remains preserved within the hydrate itself. It is highly possible that the migration of warm fluids [*Dewangan et al.*, 2011; *Mandal et al.*, 2014] during the opening of the fault may have altered the P-T conditions of unit-IV, and hence the gas hydrates in this unit may have started dissociating leading to upward migration of methane through the fault system. Simultaneously, residual H₂S might have been released by dissociating hydrates causing subsequent transformation of iron oxides and precipitation of iron sulfides (pyrite) in this unit similar to that observed by *Housen and Musgrave* [1996] in Cascadia margin. The observed depletion in magnetic susceptibility and occurrence of pyrite grains in unit-IV support our interpretations (Figure 2a, Figures 8g and 8h and Figure 9d). The other source of H₂S could be through active fluid advection from the deeper sediment strata [*Housen and Musgrave*, 1996]. Another possibility is the intrusion of seawater through the fault system which may lead to

AOM, and subsequent release of H₂S might have resulted in pyritization and dissolution of iron oxides. During late diagenesis, authigenic ferri-magnetic iron sulfides (greigite and pyrrhotite) might have been formed and trapped in gas hydrate. As hydrates dissociates, the iron sulfides are exposed and are no longer stable, and subsequently get transformed into stable pyrite [Kars and Kodama, 2015]. Therefore unit-IV may be considered as a fossil gas hydrate interval at site NGHP-01-10D. Similar occurrence of reduction of magnetic susceptibility below the BSR is also observed in NGHP-01-05 location which is also located on top of the mound with numerous fault systems [Kumar *et al.*, 2014]. Therefore, we believe that the fault system has an active role to play in the processes responsible for the dissolution of magnetic mineral. Due to limited magnetic, geochemical and sedimentological data from this unit, the genesis of low magnetic values cannot be ascertained. More detailed pore water geochemical / sedimentological data is required in the vicinity of the base of GHSZ to understand the processes related to deep pyritization.

Based on rock-magnetic, geochemical, sedimentological signatures and seismic data analysis, a conceptual model explaining the different controls on the development of gas hydrate system in the K-G basin is proposed (Figure 13). As sedimentation continued in the K-G basin, huge amount of organic matter got decomposed resulting in production of methane gas and formed a gas reservoir in unit- IV. When the P-T conditions were favourable, hydrates started forming in this zone. Later, during onset of high sedimentation event, huge amount of sediment was supplied to the basin. Hence due to high sedimentation the detrital minerals survived the early diagenesis and got buried, forming the magnetite rich zones in unit- III. As sedimentation continued, the major fault system of the K-G basin got activated, probably at the start of unit- II (which is base of unit – II). The opening of the faults altered the P-T conditions, and consequently hydrates in unit- IV might have started to dissociate and methane gas started migrating upwards and entered unit- III, thereby creating a fossil gas hydrate interval in unit- IV. Simultaneously, residual H₂S supplied by dissociating hydrates, caused subsequent transformation of iron oxides and precipitation of pyrite in this unit [Housen and Musgrave, 1996]. The supply of methane gas through the fault system might have led to the formation of the hydrate in unit – III (present day hydrate reservoir). Later, the closure of the fault system might have taken place possibly at the top of unit- II. The unit- I highlights the scenario of the present day sedimentation and geochemical conditions leading to diagenesis of detrital minerals causing dissolution of detrital Fe-Ti bearing minerals in the K-G basin.

6. Conclusion

We have demonstrated the potential of using a magnetic approach along with other sedimentological and geochemical proxies to decipher the controls on the development of the gas hydrate system in the K-G basin. This sample-based multi-proxy study was aimed at deepening fundamental understanding of geological control on evolution of gas hydrate systems which is also a prerequisite for future high-resolution mapping and modelling. The rock magnetic methods were used to characterize magnetic mineral concentration, mineralogy and grain sizes in a sediment core NGHP-01-10D from K-G basin. Four distinct sedimentary units, consisting of ferri-magnetic iron oxides and sulfides are identified. The magnetic mineralogy of different units has been confirmed by rock-magnetic, SEM-EDS and XRD data. A marked decrease in magnetic susceptibility, an abundance of pyrite grains and the relative increase in CRS concentration provide evidence of deep pyritization processes in unit-IV. Based on the variation in magnetic, geochemical and sedimentological parameters, we provided four plausible hypotheses to explain the deep pyritization processes in this unit. Our findings are summarized in a conceptual model (Figure 13) which can probably be generalized to other depositional environments.

Acknowledgement

We thank the Directors of CSIR-NIO, NIOT, NCAOR, advisor MOES, NGHP (India) for supporting this study. The NGHP coordinated by DGH is thanked for providing sediment samples of Indian National Gas Hydrate Expedition 01 for this study. Thanks to N. Satelkar, A. Khalap and V. Gaikwad for providing assistance in setting up the magnetic extraction unit. Thanks to T. Ramprasad, A. Mazumdar, A. Paropkari, S. Iyer, O.S. Chouhan, Pratima Kessarkar and Nagender Nath for their timely suggestions. Thanks to Daryl Vaz for providing technical support. Thanks to Girish Prabhu and Areef Sardar for providing assistance with XRD and SEM-EDS analysis. We would also like to thank Director, Indian Institute of Geomagnetism (IIGM), Panvel for allowing us to carry out specialized rock-magnetic measurements at the environmental magnetic laboratory. The data used in this study can be made available upon email request to the corresponding author (firoz@nio.org). We sincerely acknowledge the comments from the editors and reviewers. This is the contribution of CSIR-NIO GEOSCAPE project with publication no. 5971.

Figure captions:

Figure - 1: Map showing the sediment core location of NGHP-01-10D off Krishna-Godavari (K-G) basin, Bay of Bengal.

Figure - 2: Depth variation of selected rock-magnetic (a-d) and geochemical (e-g) data of the sediment core NGHP-01-10D. The depth of bottom simulating reflector (BSR), the position of sulphate methane transition zone (SMTZ) and gas hydrate stability zone (GHSZ) are marked. Blue and red arrows indicate the enrichment depth of chromium reducible sulfur (CRS) and Molybdenum (Mo). The sulfur isotope ratios of CRS ($\delta^{34}\text{S}_{\text{CRS}}$), Chromium (CRS) and total organic carbon (TOC) data for the NGHP-01-10D core was provided by **Peketi et al., [2012]**.

Figure - 3: (a) Hysteresis parameters displayed in a Day plot (Day, 1977) from Hole NGHP-01-10D (b) Down-core variation in magnetic grain size index parameter (D_{JH}). SD = single domain, PSD = pseudo-single domain, MD = multi-domain.

Figure - 4: Temperature dependence of magnetic susceptibility for selected samples (a) Unit-I: 1.4 mbsf (b) Unit- II: 16.5 mbsf (c) Unit- III: 52.0 mbsf (d) Unit- IV: 180.7 mbsf. A solid red line indicates heating curve and blue line indicates cooling curve.

Figure - 5: Distribution of grain size parameters and magnetic susceptibility data of NGHP-01-10D Hole. Blue lines indicate the depth of CRS enrichment and dotted line is used to separate each sedimentary unit. The symbol * marked in red indicates the peaks of increased sand content observed throughout the sediment core at depth intervals of 9.8 mbsf, 27.39 mbsf, 36.08 mbsf, 42.6 mbsf, 78.8 mbsf, 99.5 mbsf, 121.22 mbsf, 145.1 mbsf, 159.5 mbsf, 179.5 mbsf, 187.6 mbsf and 197.2 mbsf.

Figure - 6: Physical properties (a) bulk density (b) grain density (c) porosity and (d) magnetic susceptibility data of NGHP-01-10D Hole. (data provided by NGHP expedition-01 Initial reports).

Figure -7: Scanning electron microscopy on magnetic extracts from different depth intervals of NGHP-01-10D Hole. (a) and (b) unit - I: Titano-magnetite (TM) grains; (c) and (d) unit- II: framboidal pyrites (P). The arrows indicate dissolution features (mousy, etching) on magnetic grains (Fig. 7a,b) and aggregation of pyrite crystals (Fig. 7c,d). The EDS spectra of the respective grains are shown in a – c.

Figure - 8: Scanning electron microscopy on magnetic extracts from different depth intervals of NGHP-01-10D Hole. unit- III (a), (b), and (c): Fe-Ti-rich magnetic grains, (d) titanohematite

lamellae (TH) (e) thin layer of pyrite (P) coated titanomagnetite (TM) grain (f) titano-magnetite grains and in unit- IV (g) individual titanomagnetite and pyrite (P) grains (h) pyrite overgrowth on host titano-magnetite grain. The arrow in Fig. 8d indicates the complex dissolution pattern of titanohematite (TH) grain. The EDS spectra of the respective grains are shown in a – g.

Figure - 9: The XRD analysis of magnetic extracts from sediment depth intervals: a) XRD peaks at 1.4 mbsf (Unit- I) corresponds to dominant titano-magnetite (TM). (b) XRD peaks at 19.5 mbsf (Unit- II) shows mixture of TM and pyrite (P). c) The mineral peaks at 96.0 mbsf (unit- iii) shows the presence of quartz (Q), TM and P. d) XRD mineral peaks at 180.7 (mbsf) shows the presence of Q, TM and P in Unit-IV.

Figure - 10: (a-d): Bivariate scatter plots of magnetic parameters and chromium reducible sulfur (CRS) data of Hole NGHP-01-10D. Please note that the grey arrows in the scatter plots are used only to highlight the trends between magnetic and non-magnetic parameters.

Figure - 11: (a-d): Bivariate scatter plots of magnetic susceptibility, grain size and chromium reducible sulfur (CRS) data of Hole NGHP-01-10D. Please note that the grey arrows in the scatter plots are used only to highlight the trends between magnetic and non-magnetic parameters.

Figure - 12: Analysis of seismic line (a) time integral (b) interpreted seismic data with different multi-channel seismic data. Gas hydrate-bearing layer (L1-L4) , three major faults (F1-F3) and the interpreted bottom simulating reflector (BSR) and gas layers (c) throws of the faults across interpreted gas horizons L1,L2,L3 (F1~50 m) (F3~35 m) (modified from Dewangan et al., 2011).

Figure - 13: A conceptual model explaining the evolution of gas hydrate system in the K-G basin. All findings that explains different stages of evolution of methane hydrate system at the studied site are summarized.

References:

- Bastia, R. (2007), Geological setting and petroleum systems of India's east coast offshore basins: concepts and applications, Technology, Publications, Dehradun, India, 204, Eastern Book, Delhi, India.
- Berner, R.A. (1970), Sedimentary pyrite formation, *American Journal of Science.*, 268 (1), 1–23.
- Berner, R. A. (1984), Sedimentary pyrite formation: An update, *Geochim. Cosmochim. Acta.*, 48, 605–615, doi:10.1016/0016-7037(84)90089-9.
- Biksham, G., and V. Subramanian (1988), Sediment transport of the Godavari River basin and its controlling factors, *J. Hydrol.*, 101, 275–290, doi:10.1016/0022-1694(88)90040-6.
- Borowski, W. S., C. K. Paull, and W. Ussler III (1996), Marine pore-water sulfate profiles indicate in situ methane flux from underlying gas hydrate, *Geol.*, 24(7), 655-658, doi: 10.1130/0091-7613.
- Boswell, R. and T. S. Collett (2011), Current perspectives on gas hydrate resources, *Energy Environ. Sci.*, 4, 1206-1215, doi: 10.1039/C0EE00203H.
- Canfield, D.E. (1991), Sulfate reduction in deep-sea sediments, *American Journal of Science.*, 291 (2), 177–188.
- Chang, L., A. P. Roberts, W. Williams, J. D. Fitz Gerald, J. C. Larrasoana, L. Jovane, and A. R. Muxworthy (2012), Giant magnetofossils and hyperthermal events, *Earth Planet. Sci. Lett.*, 351–352, 258–269, doi:10.1016/j.epsl.2012.07.031.
- Channell, J.E.T. and T. Hawthorne (1990). Progressive dissolution of titanomagnetites at ODP Site 653 (Tyrrhenian Sea), *Earth Planet. Sci. Lett.*, 96, 469–480.
- Clennell, M. B., M. Hovland, J. S. Booth, P. Henry, and W. J. Winters (1999), Formation of natural gas hydrates in marine sediments: 1. Conceptual model of gas hydrate growth conditioned by host sediment properties, *J. Geophys. Res.*, 104, 22985–23004, doi: 10.1029/1999JB900175.
- Choudhori, M., D. Guha, A. Dutta, S. Sinha, and N. Sinha (2011), Spatiotemporal Variations and Kinematics of Shale Mobility in the Krishna-Godavari Basin, India, *In AAPG Memoir 93 Shale Tectonics*, Ed. Wood, L.H., 91-110, doi:10.1306/13231310M933420.
- Collett, T., M. Riedel, J. R. Cochran, R. Boswell, J. Presley, P. Kumar, A. Sathe, M. Lall, V. Sibal, and the NGHP Expedition 01 Scientists (2008), Indian National Gas Hydrate Program, Expedition - 01, Initial report, Directorate General of Hydrocarbons, Ministry of Petroleum and Natural gas, India.
- Cornell, R. and U. Schwertmann (2003), *The Iron Oxides: Structures, Properties, Reactions, Occurrences and Uses*, 2nd ed. Wiley-VCH, Weinheim.
- Damuth, J. E. (1994), Neogene gravity tectonics and depositional processes on the deep Niger Delta continental margin, *Mar. Pet. Geol.*, 11, 320-346, doi:10.1016/0264-8172(94)90053-1.
- Day, R., M. Fuller, and V. A. Schmidt (1977), Hysteresis properties of titanomagnetites: Grain size and compositional dependence, *Phys. Earth Planet. Inter.*, 13, 260–267.

Dekkers, M.J. (1997), Environmental magnetism: An introduction, *Geologie en Mijnbouw* 76, 163–182, doi:10.1023/A:1003122305503.

Dewangan, P., T. Ramprasad, M. V. Ramana, A. Mazumdar, M. Desa, and F. K. Badesab (2010), Seabed morphology and gas venting features in the continental slope region of Krishna-Godavari basin, Bay of Bengal: implications in gas-hydrate exploration, *Mar. Pet. Geol.*, 27 (7), 1628–1641, doi:10.1016/j.marpetgeo.2010.03.015.

Dewangan, P., G. Sriram, T. Ramprasad, M. V. Ramana, and P. Jaiswal (2011), Fault system and thermal regime in the vicinity of site NGHP-01-10, Krishna–Godavari basin, Bay of Bengal, *Mar. Petrol. Geol.*, 28,1899–1914, doi:10.1016/j.marpetgeo.2011.03.009.

Dewangan, P., N. Basavaiah, F. K. Badesab, A. Usapkar, A. Mazumdar, R. Joshi, and T. Ramprasad (2013), Diagenesis of magnetic minerals in a gas hydrate/cold seep environment off the Krishna–Godavari basin, Bay of Bengal, *Mar. Geo.*, 340, 57–70, doi:10.1016/j.margeo.2013.04.016.

Dewangan, P., R. Mandal, P. Jaiswal, T. Ramprasad, and G. Sriram (2014), Estimation of seismic attenuation of gas hydrate bearing sediments from multi-channel seismic data: A case study from Krishna-Godavari offshore basin, *Mar. Petrol. Geol.*, 58, 356-367.

Egawa, K., O. Nishimura, S. Izumi, E. Fukami, Y. Jin, M. Kida, Y. Konno, J. Yoneda, T. Ito, K. Suzuki, Y. Nakatsuka, and J. Nagao (2015), Bulk sediment mineralogy of gas hydrate reservoir at the East Nankai offshore production test site, *Mar. Pet. Geol.*, 66, 379-387.

Enkin, R. J., J. Baker, D. Nourgaliev, P. Iassonov, and T. S. Hamilton (2007), Magnetic hysteresis parameters and Day plot analysis to characterize diagenetic alteration in gas-hydrate-bearing sediments, *J. Geophys. Res.*, 112, B06S90, doi:10.1029/2006JB004638.

Esteban, L., R. Enkin, and T. Hamilton (2008), Gas hydrates and magnetism: Surveying and diagenetic analysis., Proceedings of the 6th International Conference on Gas Hydrates (ICGH 2008), Vancouver, British Columbia, Canada.

Evans, M.E. and Heller, F (2003), Environmental Magnetism: Principles and Applications of Enviromagnetism, 86. International Geophysics Series. Academic Press, New York, 293pp.

Fu, Y., T. Von Dobeneck, C. Franke, D. Heslop, and S. Kasten (2008), Rock-magnetic identification and geochemical process models of greigite formation in Quaternary marine sediments from the Gulf of Mexico (IODP Hole U1319A), *Earth and Planetary Sci. Lett.*, 275(3-4), 233-245, doi:10.1016/j.epsl.2008.07.034.

Ginsburg, G., V. Soloviev, T. Matveeva, and I. Andreeva (2000), Sediment grain size control on gas hydrate presence, Sites 994, 995, and 997, In Paull, C. K., Matsumoto, R., Wallace, P.J., and Dillon, W.P. (Eds), *Proc. ODP. Sci. Results*, 164, College Station, Texas, Ocean Drilling Program, p. 237–245, doi:10.2973/odp.proc.sr.164.236.2000.

Haacke, R. R., G. K. Westbrook, and M. S. Riley (2008), Controls on the formation and stability of gas hydrate-related bottom-simulating reflectors (BSRs): a case study from the west Svalbard continental slope, *J. Geophys. Res.*, 113, B05104, doi: 0.1029/2007JB005200.

Heslop, D., A. P. Roberts, L. Chang, M. Davies, A. Abrajevitch, and P. De Deckker (2013), Quantifying magnetite magnetofossil contributions to sedimentary magnetizations, *Earth Planet. Sci. Lett.*, 382, 58–65.

Hesse, R. (2003), Pore water anomalies of submarine gas hydrate zones as tool to assess hydrate abundance and distribution in the subsurface: What have we learned in the past decade?, *Earth-Sci. Rev.*, 61, 149–179, doi:10.1016/S0012-8252(02)00117-4.

Hornig, C. S. and K. H. Chen (2006), Complicated magnetic mineral assemblages in marine sediments offshore of southwestern Taiwan: possible influence of methane flux on the early diagenetic process, *Terr. Atmos. Ocean. Sci.*, 17(4), 1009-1026.

Hornig, C.S. and A. P. Roberts (2006), Authigenic or detrital origin of pyrrhotite in sediments? Resolving a paleomagnetic conundrum, *Earth and Planetary Sci. Lett.*, 241, 750–762.

Hounslow, M. W., and B. A. Maher (1996), Quantitative extraction and analysis of carriers of magnetization in sediments, *Geophys. J. Int.*, 124, 57 – 74.

Housen, B.A. and R. J. Musgrave (1996), Rock-magnetic signature of gas hydrates in accretionary prism sediments, *Earth and Planetary Sci. Lett.*, 139 (3–4), 509–519.

Jaiswal, P., P. Dewangan, T. Ramprasad, and C. Zelt (2012a), Seismic characterization of hydrates in faulted, fine-grained sediments of Krishna-Godavari basin: Unified imaging, *J. Geophys. Res.*, 117, B04306, doi: 10.1029/2011JB009024.

Jaiswal, P., P. Dewangan, T. Ramprasad, and C. Zelt (2012b), Seismic characterization of hydrates in faulted, fine-grained sediments of Krishna-Godavari Basin: Full waveform inversion, *J. Geophys. Res.*, 117, B10305, doi: 10.1029/2012JB009201.

Jørgensen, B. B., M. E. Böttcher, H. Lüschen, L. N. Neretin, and I. I. Volkov (2004), Anaerobic methane oxidation and a deep H₂S sink generate isotopically heavy sulfides in Black Sea sediments, *Geochim et Cosmochim Acta.*, 68(9), 2095-2118, doi:10.1016/j.gca.2003.07.017.

Joshi., R. K. Joshi, A. Mazumdar, A. Peketi, P. B. Ramamurty, B. G. Naik , M. Kocherla ,Mary Ann Carvalho, P. Mahalakshmi, P. Dewangan, and M. V. Ramana (2014), Gas Hydrate destabilization and methane release events in the Krishna-Godavari Basin, Bay of Bengal, *Mar. Pet. Geol.*, 58, 476-489, doi:10.1016/j.marpetgeo.2014.08.013.

Karlin, R., and S. Levi (1985), Geochemical and sedimentological control of the magnetic properties of hemipelagic sediments, *J. Geophys. Res.*, 90(B12), 10373-10392. doi: 10.1029/JB090iB12p10373.

Kars, M. M. and K. Kodma (2015), Authigenesis of magnetic minerals in gas hydrate bearing sediments in the Nankai Trough, Offshore Japan, *Geochem, Geophys, Geosyst.*, 16, 947-961,doi: 10.1002/2014GC005614.

Kasten, S., T. Freudenthal, F. X. Gingele, and H. D. Schulz (1998), Simultaneous formation of iron-rich layers at different redox boundaries in sediments of the Amazon deep-sea fan, *Geochim, Cosmochim Acta.*, 62, 2253-2264, doi:10.1016/S0016-7037(98)00093-3.

Kirschvink, J. L. and S. R. Chang (1984), Ultrafine-grained magnetite in deep sea sediments: Possible bacterial magnetofossils, *Geology.*, 12, 559-562.

Knittel, K. and A. Boetius (2009), Anaerobic oxidation of methane: progress with an unknown process, *Annu. Rev. Microbiol.*, *63*, 311-334.

Kocherla, M., B. M. A. Teichert, S. Pillai, M. Satyanarayanan, P. B. Ramamurty, D. J. Patil, and A. N. Rao (2015), Formation of methane-related authigenic carbonates in a highly dynamic biogeochemical system in the Krishna–Godavari basin, Bay of Bengal, *Mar. Pet. Geol.*, *64*, 324–333, doi:10.1016/j.marpetgeo.2015.02.034.

Kumar P., T. S. Collett, R. Boswell, J. R. Cochran, M. Lall, A. Mazumdar, M. V. Ramana, T. Ramprasad, M. Riedel, K. Sain, A. V. Sathe, and K. Vishwanath (2014), the NGHP Expedition 01 Scientific Party Geologic implications of gas hydrates in the offshore of India: Krishna–Godavari basin, Mahanadi basin, Andaman Sea, Kerala–Konkan Basin, *Mar. Pet. Geol.*, *58*, Part A, 3–28, doi:10.1016/j.marpetgeo.2014.07.031.

Kvenvolden, K. (1993), Gas hydrates-Geological perspective and global change, *Rev Geophysics.*, *31*, 173–187, doi: 10.1029/93RG00268.

Larrasoña, J.C., A. P. Roberts, R. J. Musgrave, E. Gràcia, E. Piñero, M. Vega, and F. Martínez Ruiz (2007), Diagenetic formation of greigite and pyrrhotite in gas hydrate marine sedimentary systems. *Earth and Planetary Sci. Lett.*, *261*, (3–4), 350–366.

Leslie, B.W., D. E. Hammond, W. M. Berelson, and S. P. Lund (1990), Diagenesis in anoxic sediments from the California continental borderland and its influence on iron, sulfur, and magnetite behaviour, *J. Geophys. Res.*, *95*(B4), 4453-4470, doi: 10.1029/JB095iB04p04453.

Lee M. W. and T. S. Collett (2009), Gas hydrate saturations estimated from fractured reservoir at site NGHP-01-10, Krishna–Godavari basin, India, *J. Geophys. Res.*, *114*, pp. 1–13 B07102, doi: 10.1029/2008JB006237.

Liu, J., R. Zhu, A. P. Roberts, S. Li, and J. H. Chang (2004), High-resolution analysis of early diagenetic effects on magnetic minerals in post-middle-Holocene continental shelf sediments from the Korea Strait, *J. Geophys. Res.*, *109*(B3), B03103, doi: 10.1029/2003JB002813.

Lorenson, T. (2000), Microscopic character of marine sediment containing disseminated gas hydrate: Examples from the Blake Ridge and the Middle America Trench, *N.Y acad. Sci.*, *912*, 189-194.

Lowe, C., R. J. Enkin, J. Baker, and S. R. Dallimore (2005), Investigation of airborne magnetic data and magnetic properties of cored rocks from the Mallik gas hydrate field, in Scientific Results from the Mallik 2002 Gas Hydrate Production Research Well Program, Mackenzie Delta, Northwest Territories, *Geol. Surv. Can. Bull.*, *585*.

Mandal, R., P. Dewangan, T. Ramprasad, B.J.P. Kumar, and K. Vishwanath (2014), Effect of thermal non-equilibrium, seafloor topography and fluid advection on BSR-derived geothermal gradient, *Mar. Pet. Geol., Part A*, 368-381.

Mazumdar, A., P. Dewangan, H. M. João, A. Peketi, V. R. Khosla, M. Kocherla, F. K. Badesab, R. K. Joshi, P. Roxanne, P. B. Ramamurty, S. M. Karisiddaiah, D. J. Patil, A. M. Dayal, T. Ramprasad, C. J. Hawkesworth, and R. Avanzinelli (2009), Evidence of paleo-cold seep activity from the Bay of Bengal, offshore India, *Geochem, Geophys, Geosyst.*, *10*, doi: 10.1029/2008GC002337.

Mazurenko, L. L., V. A. Soloviev, J. M. Gardner, and M. K. Ivanov (2003), Gas hydrates in the Ginsburg and Yuma mud volcano sediments (Moroccan margin): Results of chemical and isotopic studies of pore water, *Mar. Geol.*, 195 (1–4), 201–210, doi:10.1016/S0025-3227(02)00688-6.

Milkov, A. (2004), Global estimates of hydrate-bound gas in marine sediments: how much is really out there?, *Earth. Sci. Rev.*, 66, 183-197, doi: 10.1016/j.earscirev.2003.11.002.

Musgrave, R.J., N.L. Bangs, J.C., Larrasoana, E. Gràcia, J.A., Hollamby, and M.E.Vega (2006), Rise of the base of the gas hydrate zone since the last glacial recorded by rock magnetism, *Geology.*, 34 (2), 117–120.

Neumann, T., N. Rausch, T. Leipe, O. Dellwig, Z. Berner, and M. E. Böttcher (2005), Intense pyrite formation under low-sulfate conditions in the Achterwasser lagoon, SW Baltic Sea, *Geochim. Cosmochim. Acta.*, 69, 3619–3630, doi:10.1016/j.gca.2005.02.034.

Novosel, I., G. D. Spence, and R. D. Hyndman (2005), Reduced magnetization produced by increased methane flux at a gas hydrate vent, *Mar. Geol.*, 216(4), 265-274. doi:10.1016/j.margeo.2005.02.027.

Nowaczyk, N. R.(2011), Dissolution of titanomagnetite and sulphidization in sediments from Lake Kinneret, *Israel Geophysical Journal International.*, 187, 34-44.

Peketi, A., A. Mazumdar, R. K. Joshi, D. J. Patil, P. L. Srinivas, and A. M. Dayal (2012), Tracing the paleo sulfate–methane transition zones and H₂S seepage events in marine sediments: an application of C-S-Mo systematics, *Geochem, Geophys, Geosyst.*, 13 (10), doi: 10.1029/2012GC004288.

Petersen, N., T. Von Dobeneck, and H. Vali (1986), Fossil bacterial magnetite in deep-sea sediments from the South Atlantic Ocean, *Nature.*, 320, 611-615, doi: 10.1038/320611a0.

Poulton, S.W., M.D. Krom, and R. Raiswell (2004), A revised scheme for the reactivity of iron (oxyhydr)oxide minerals toward dissolved sulphide, *Geochimica et Cosmochimica Acta.*, 68, 3703–3715. doi:10.1016/j.gca.2004.03.012.

Prabhakar, K. N., and P. L. Zutshi (1993), Evolution of Southern Part of Indian East Coast basins, *J. Geol. Soc. India.*, 41(3), 215-230.

Ramesh R. and V. Subramanian (1988), Temporal, spatial and size variation in the sediment transport in the Krishna River basin, India, *J. Hydrol.*, 98, 53–65.

Ramana, M. V., T. Ramprasad, and M. Desa (2001), Seafloor spreading magnetic anomalies in the Enderby basin, East Antarctic, *Earth Planet. Sci. Lett.*, 191 (3-4), 241-255, doi: 10.1016/S0012-821X (01)00413-7.

Ramprasad, T., P.Dewangan, M.V. Ramana, A. Mazumdar, S.M. Karisiddaiah, E.R. Ramya, and G. Sriram (2011), Evidence of slumping/sliding in Krishna–Godavari offshore basin due to gas/fluid movements, *Mar. Pet. Geol.*, 28, 1806–1816.

Rao, D. G. (2001), Sedimentation, stratigraphy, and petroleum potential of Krishna-Godavari basin, east coast of India, *AAPG Bull.*, 85, 1623–1643.

Reidinger, N., K. Pfeifer, S. Kasten, J. F. L. Garming, C. Vogt, and C. Hensen (2005), Diagenetic alteration of magnetic signals by anaerobic oxidation of methane related to a change in sedimentation rate, *Geochim et Cosmochim Acta.*, 69, 4117-4126, doi:10.1016/j.gca.2005.02.004.

Riedel M., T. S. Collett, P. Kumar, A.V. Sathe, and A. Cook (2010), Seismic imaging of a fractured gas hydrate system in the Krishna–Godavari basin offshore India, *Mar. Pet. Geol.*, 27, 1476–1493, doi:10.1016/j.marpetgeo.2010.06.002.

Roberts, A. P., L. Chang, D. Heslop, F. Florindo, and J. C. Larrasoana (2012), Searching for single domain magnetite in the ‘pseudo-singledomain’ sedimentary haystack: Implications of biogenic magnetite preservation for sediment magnetism and relative paleointensity determinations, *J. Geophys. Res.*, 117, B08104, doi:10.1029/2012JB009412.

Roberts A.P. (2015), Magnetic mineral diagenesis, *Earth Sci. Rev.*, 151, 1-47, doi:10.1016/j.earscirev.2015.09.010.

Sangode, S. J., R. Sinha, B. Phartiyal, O. S Chauhan, R. K. Mazari, T. N. Bagati, N. Suresh, S. Mishra, R. Kumar, and P. Bhattacharjee (2007), Environmental magnetic studies on some quaternary sediments of varied depositional settings in the Indian sub-continent, *Quaternary International.*, 159, 102–118, doi:10.1016/j.quaint.2006.08.015.

Shankar, U., and M. Riedel (2010), Seismic and heat flow constraints from the gas hydrate system in the Krishna-Godavari basin, India, *Mar. Geol.*, 276(1-4), 1-13, doi:10.1016/j.margeo.2010.06.006.

Simonetti, A., J. H. Knapp, K. Sleeper, C. B. Lutken, L. Macelloni, and C. C. Knapp (2013), Spatial distribution of gas hydrates from high-resolution seismic and core data, Woolsey Mound, Northern Gulf of Mexico, *Mar. Pet. Geol.*, 44, 21–33, doi:10.1016/j.marpetgeo.2013.04.004.

Sloan, E. D. Jr. (1998), Clathrate hydrates of natural gases, Marcel Dekker Inc, New York, NY, 2nd edn.

Snowball, I. F. (1993), Geochemical control of magnetite dissolution in subarctic lake sediments and the implications for environmental magnetism, *J. Quat Sci.*, 8(4), 339-346.

Soloviev, V. A. and G. D. Ginsburg (1997), Water segregation in the course of gas hydrate formation and accumulation in submarine gas-seepage fields, *Mar. Geol.*, 137, 59–68. doi:10.1016/S0025-3227(96)00079-5.

Stolz, J. F., S.B.R. Chang, and J. L. Kirschvink (1986), Magnetotactic bacteria and single-domain magnetite in hemipelagic sediments, *Nature.*, 321, 849-851, 1986.

Teichert, B. M. A., J. E. Johnson, E. A. Solomon, L. Giosan, K. Rose, M. Kocherla, E. C. Connolly, and M. E. Torres (2014), Composition and origin of authigenic carbonates in the Krishna-Godavari and Mahanadi basins, Eastern continental margin of India, *Mar. Pet. Geol.*, 58, 438-460, doi:10.1016/j.marpetgeo.2014.08.023.

Thompson, R., and F. Oldfield (1986), Environmental magnetism, Allen and Unwin., London. 227pp.

Torres M. E., A. M. Tréhu, N. Cespedes, M. Kastner, U. G. Wortmann, J. H. Kim, P. Long, A. Malinverno, J. W. Pohlman, M. Riedel, and T. S. Collett (2008), Methane hydrate formation in turbidite sediments of northern Cascadia, IODP Expedition 311, *Earth Planet. Sci. Lett.*, 271, 170–180, doi:10.1016/j.epsl.2008.03.061.

Ussler, W., and C. K. Paull (2008), Rates of anaerobic oxidation of methane and authigenic carbonate mineralization in methane-rich deep-sea sediments inferred from models and geochemical profiles, *Earth Planet. Sci. Lett.*, 266(3–4), 271–287, doi:10.1016/j.epsl.2007.10.056.

Vali, H., O. Forster, G. Amarantidis, and N. Petersen (1987), Magnetotactic bacteria and their magnetofossils in sediments, *Earth Planet. Sci. Lett.*, 86, 389-400, 1987.

Verosub, K.L. (1977). Depositional and Post depositional Processes in the Magnetization of Sediments, *Rev Geophy Space Phys.*, 15(2),129-143.

Verosub, K. and A.P. Roberts (1995), Environmental magnetism: past, present and future, *J. Geophy Res.*, 100, 2175–2192.

Winters, W.J. (2011), Physical and geotechnical properties of gas-hydrate bearing sediment from offshore India and the northern Cascadia Margin compared to other hydrate reservoir, Proceedings of the 7th International Conference on Gas Hydrates (ICGH 2011), Edinburgh, Scotland, United Kingdom, July 17-21.

Wu, S. and A.W. Bally (2000), Slope Tectonics-comparisons and Contrasts of Structural Styles of Salt and Shale Tectonics of the Northern Gulf of Mexico with Shale Tectonics of Offshore Nigeria in Gulf of Guinea, *Atlantic rifts and continental margins.*, 115, 151-172, doi: 10.1029/GM115p0151.

Xu, W., and C. Ruppel (1999), Predicting the occurrence, distribution, and evolution of methane gas hydrate in porous marine sediments, *J. Geophys. Res.*, 104(B3), 5081–5095, doi:10.1029/1998JB900092.

Yamazaki, T., A.L. Abdeldayem, and K. Ikehara (2003), Rock-magnetic changes with reduction diagenesis in Japan Sea sediments and preservation of geomagnetic secular variation in inclination during the last 30,000 years, *Earth Planet Space.*, 55, 327–340

Figure. 1

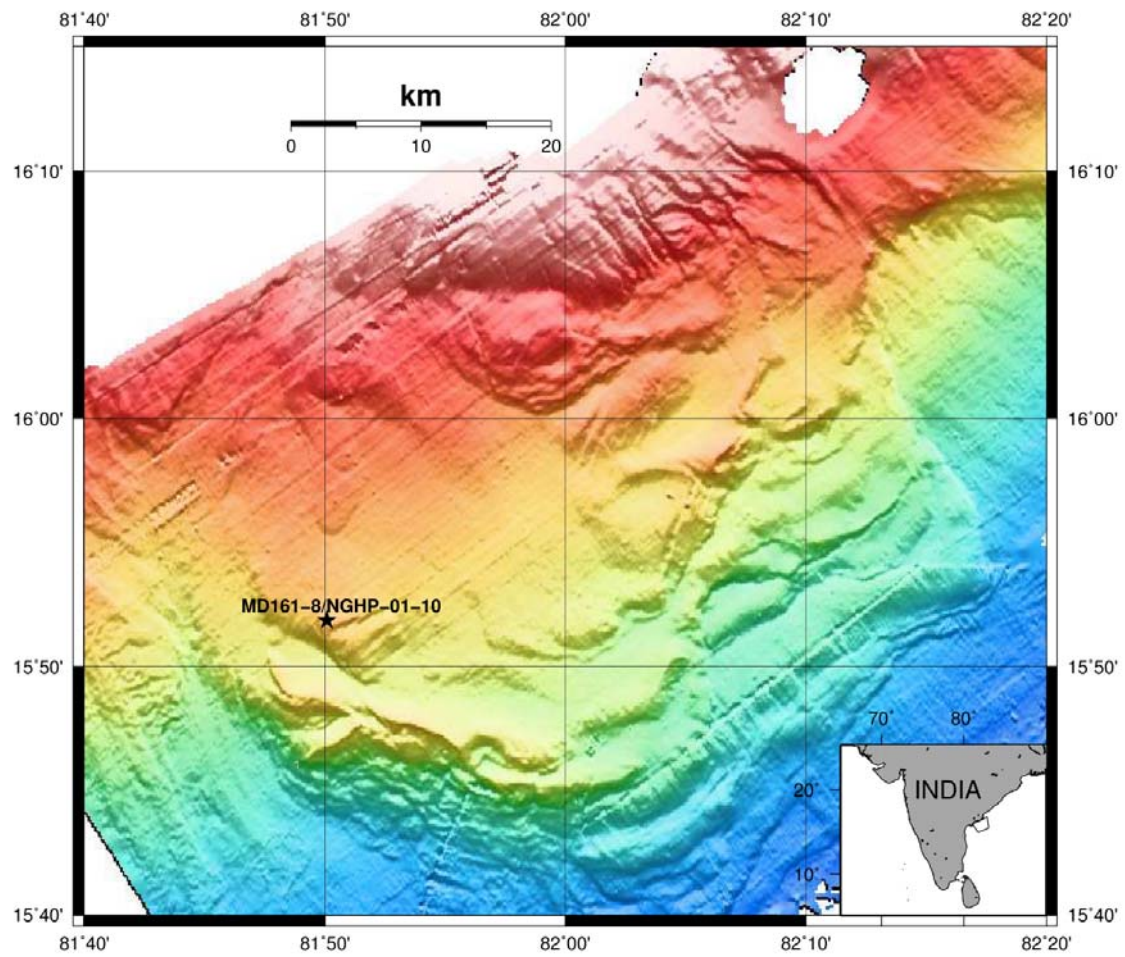


Figure 2

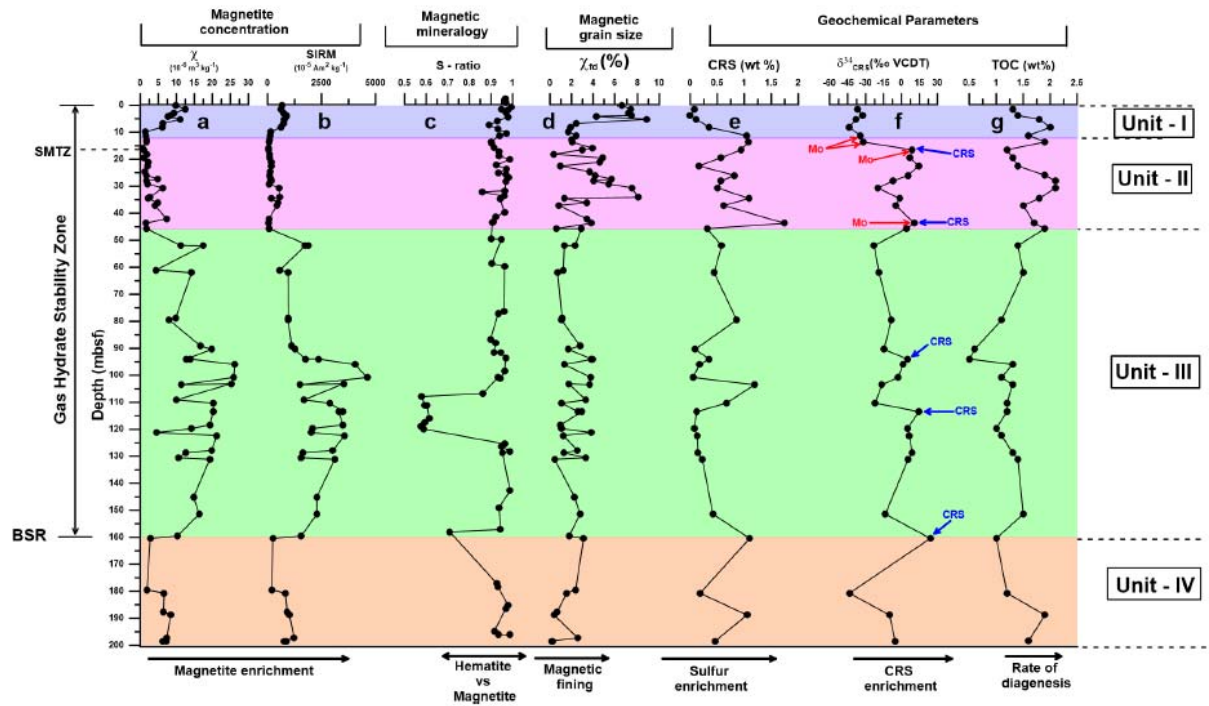


Figure 3

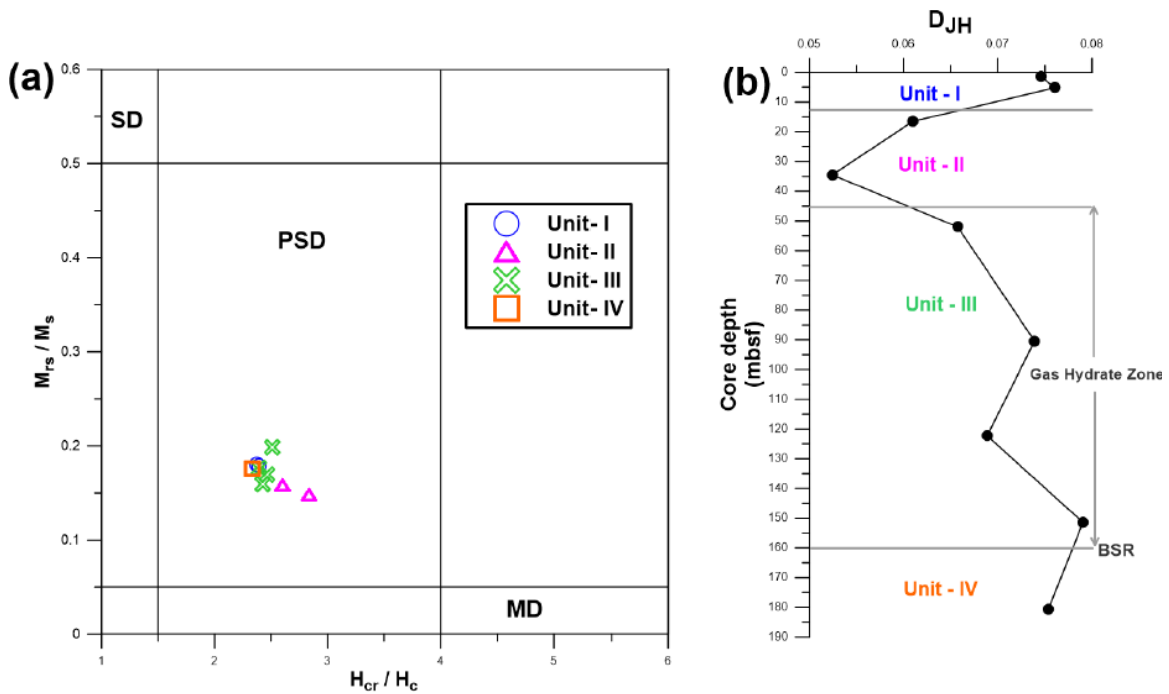


Figure 4

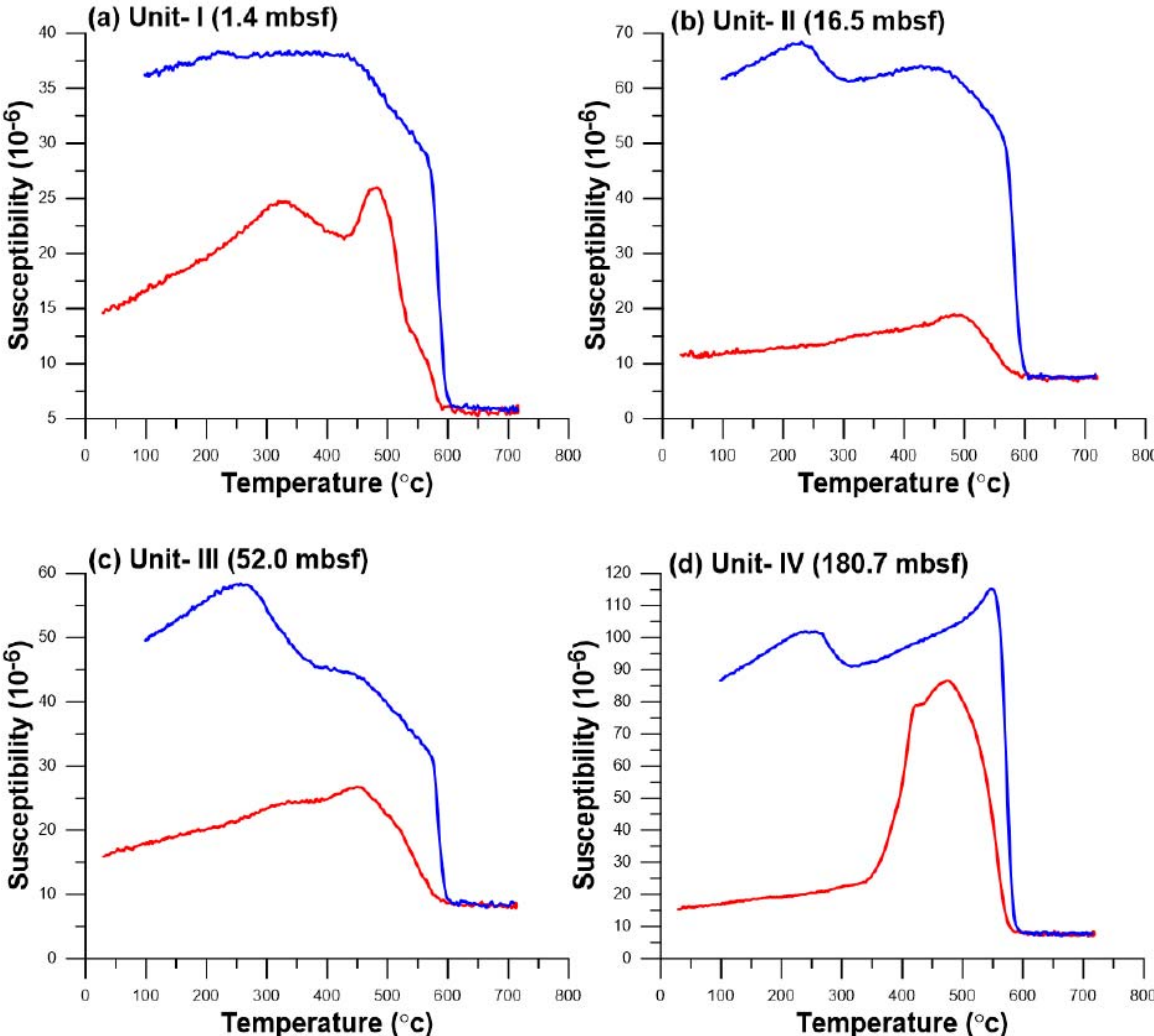


Figure 5

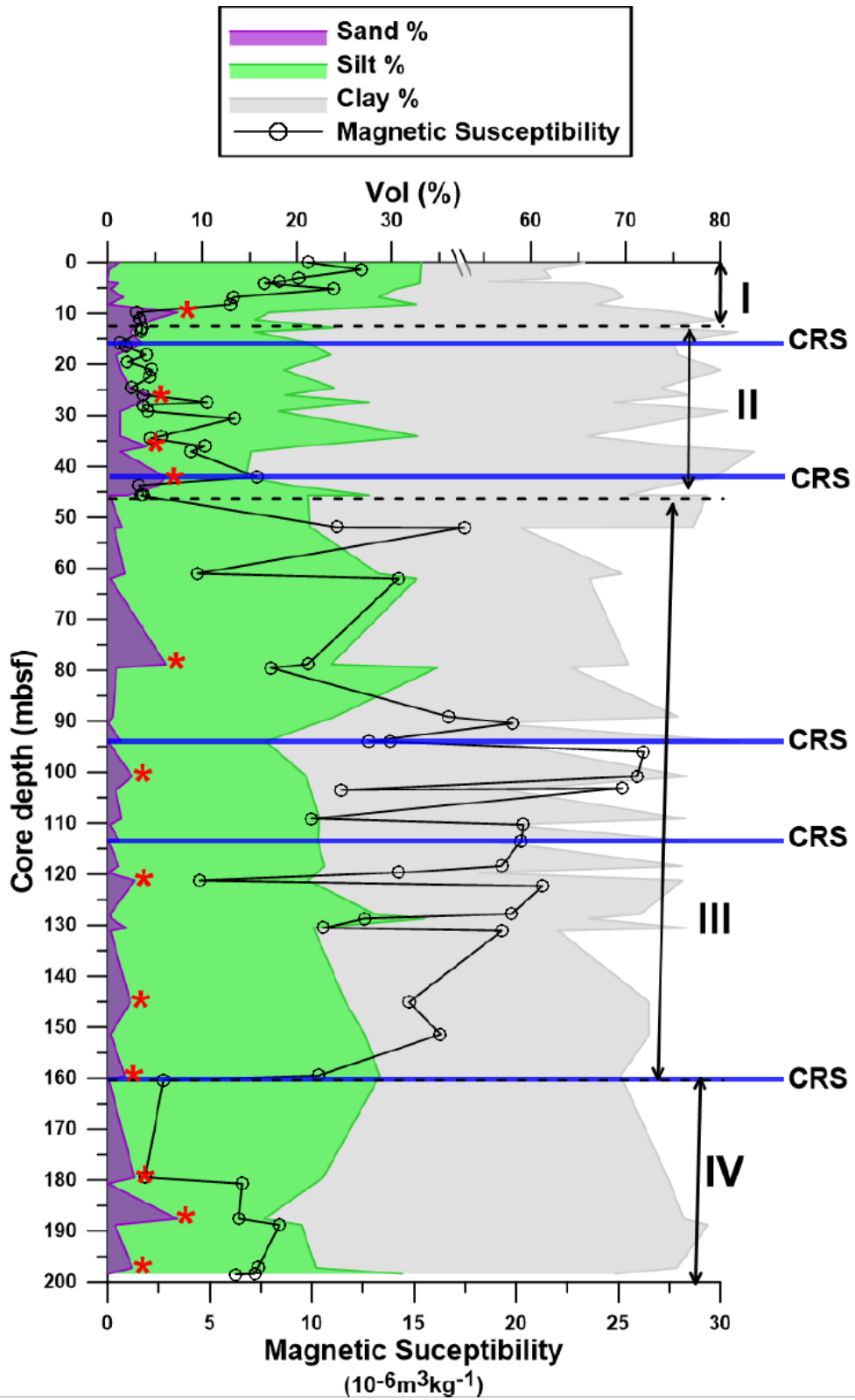


Figure 6

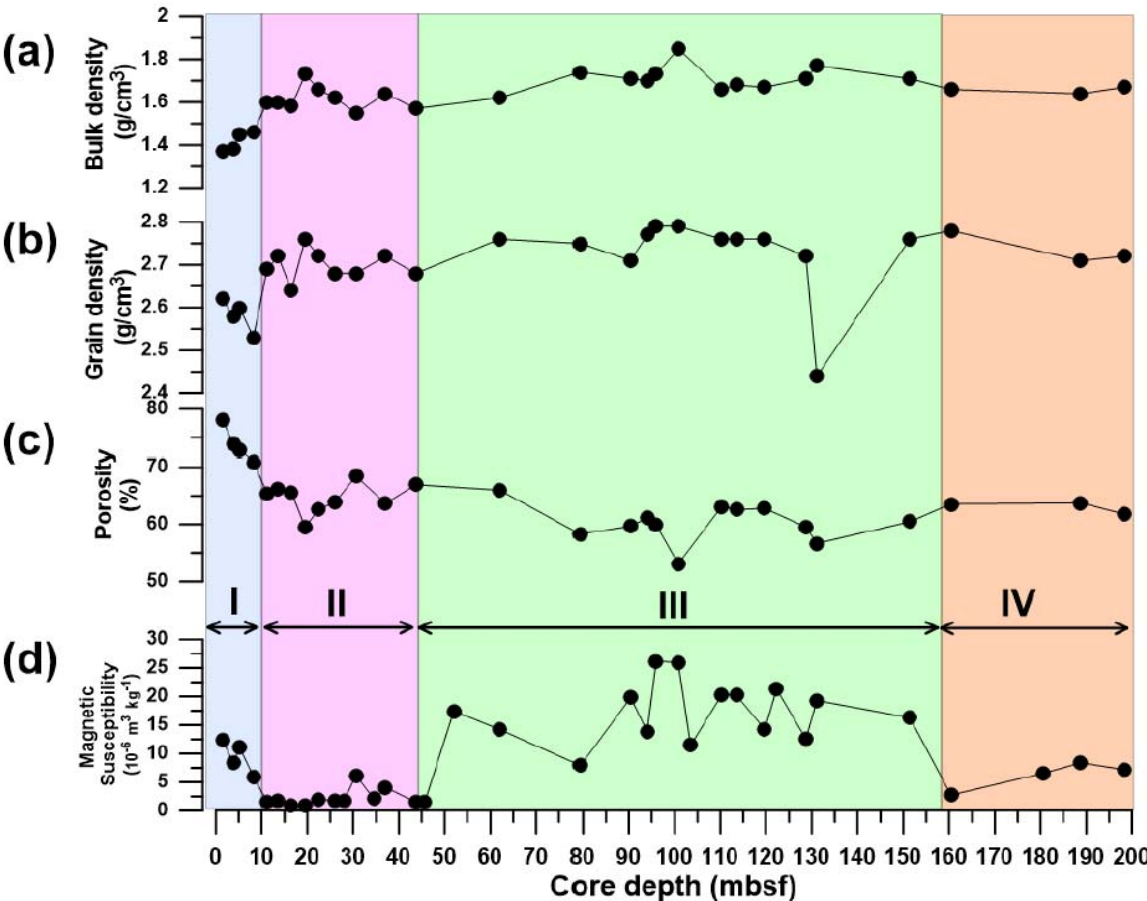


Figure 7

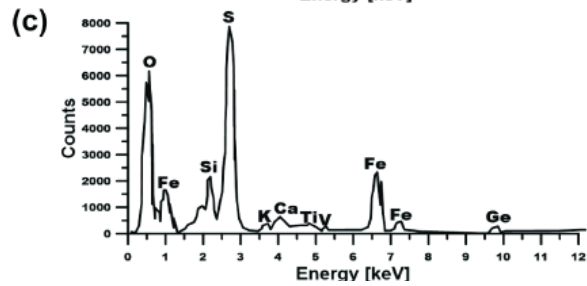
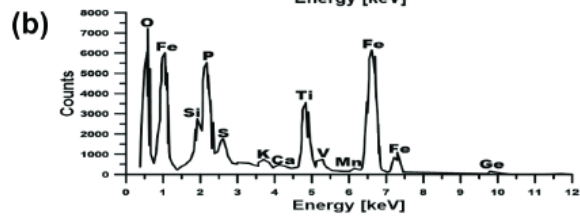
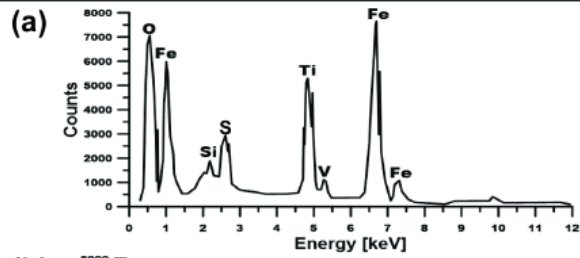
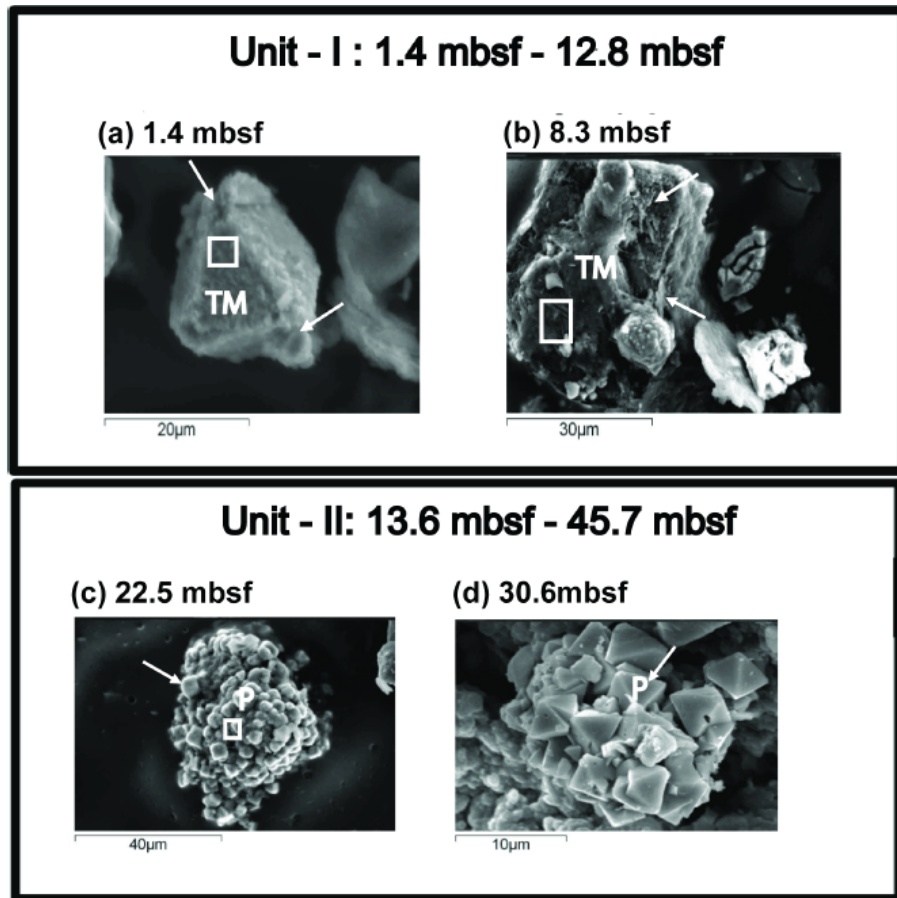


Figure 8

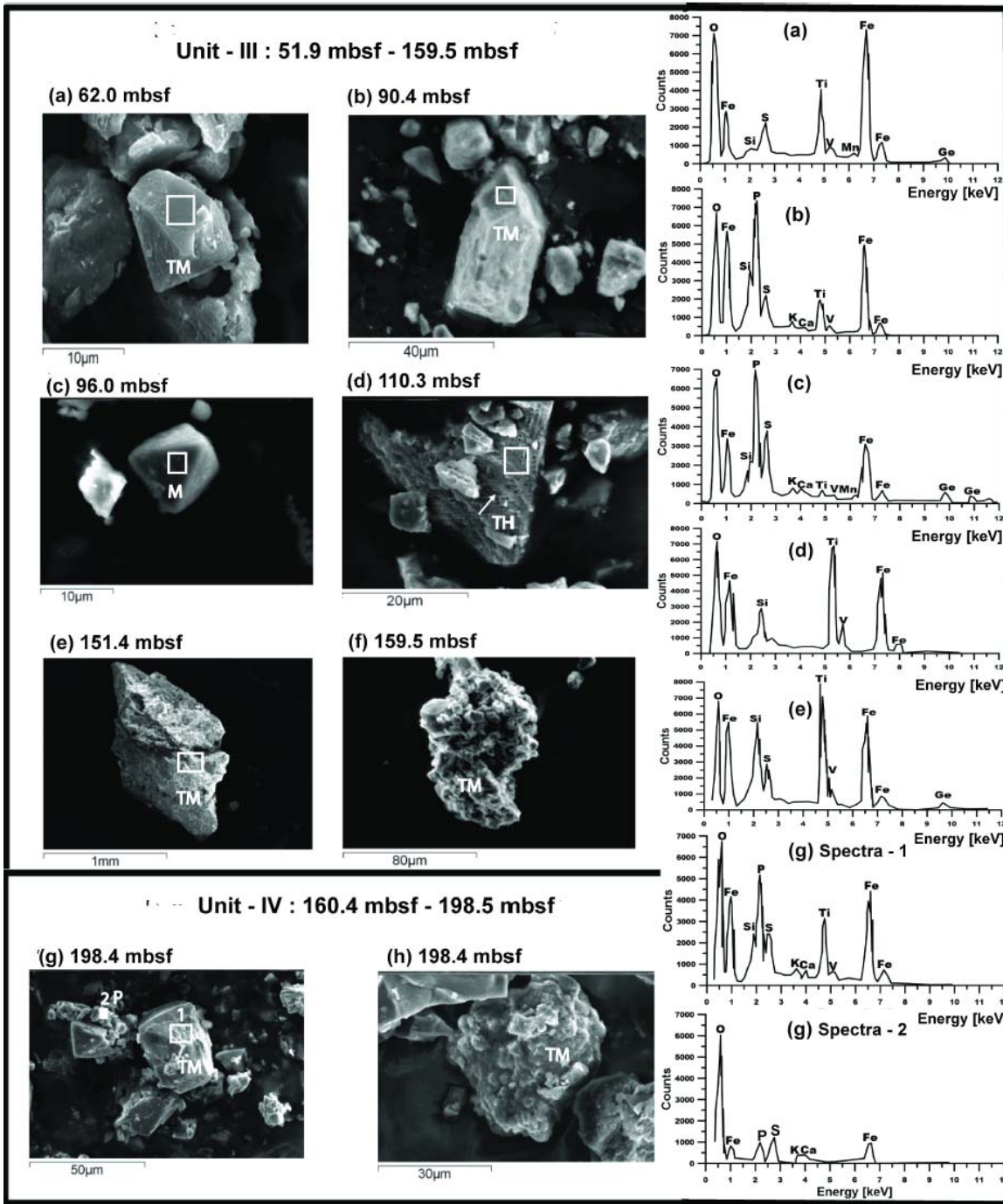


Figure 9

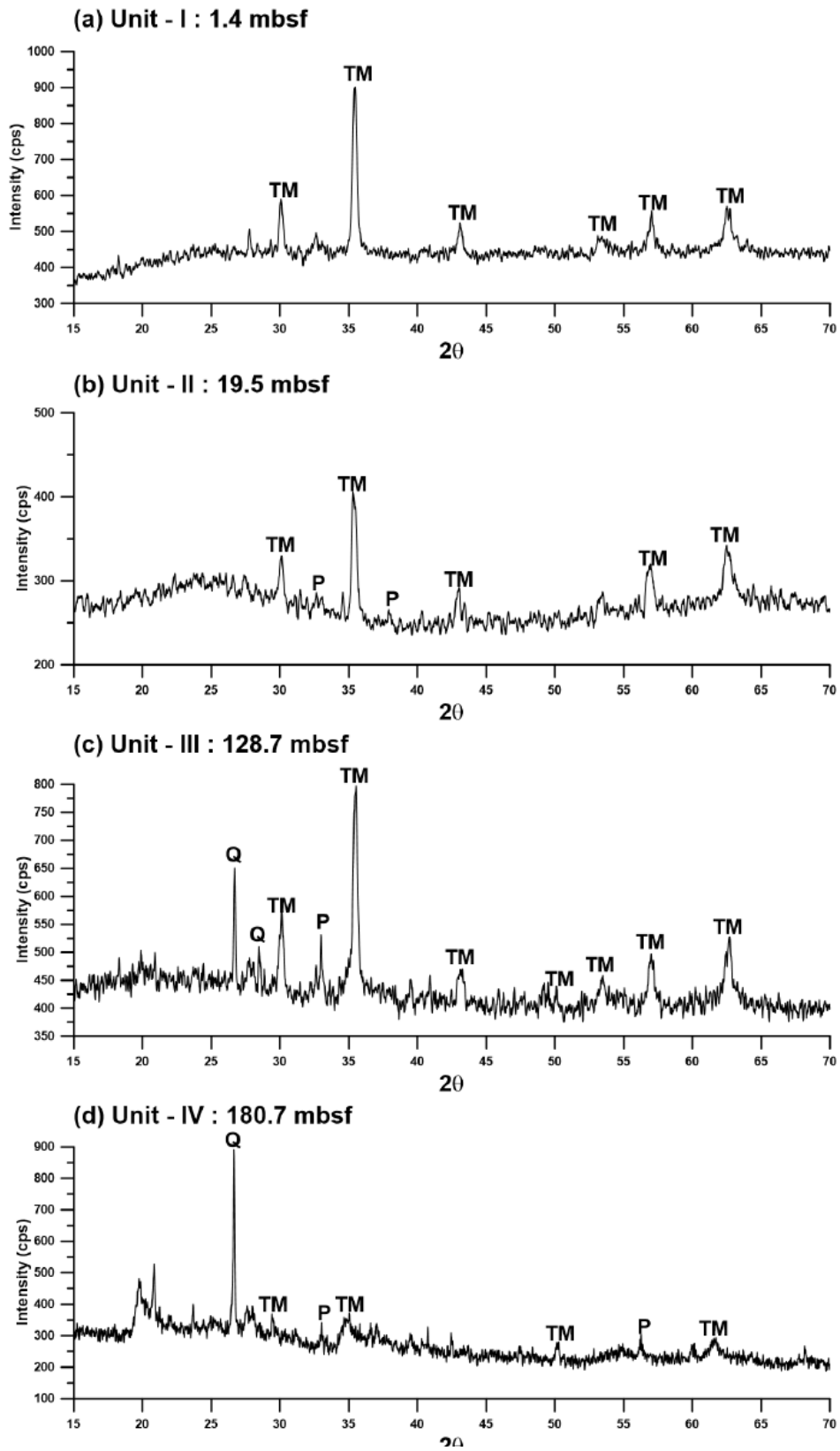


Figure 10

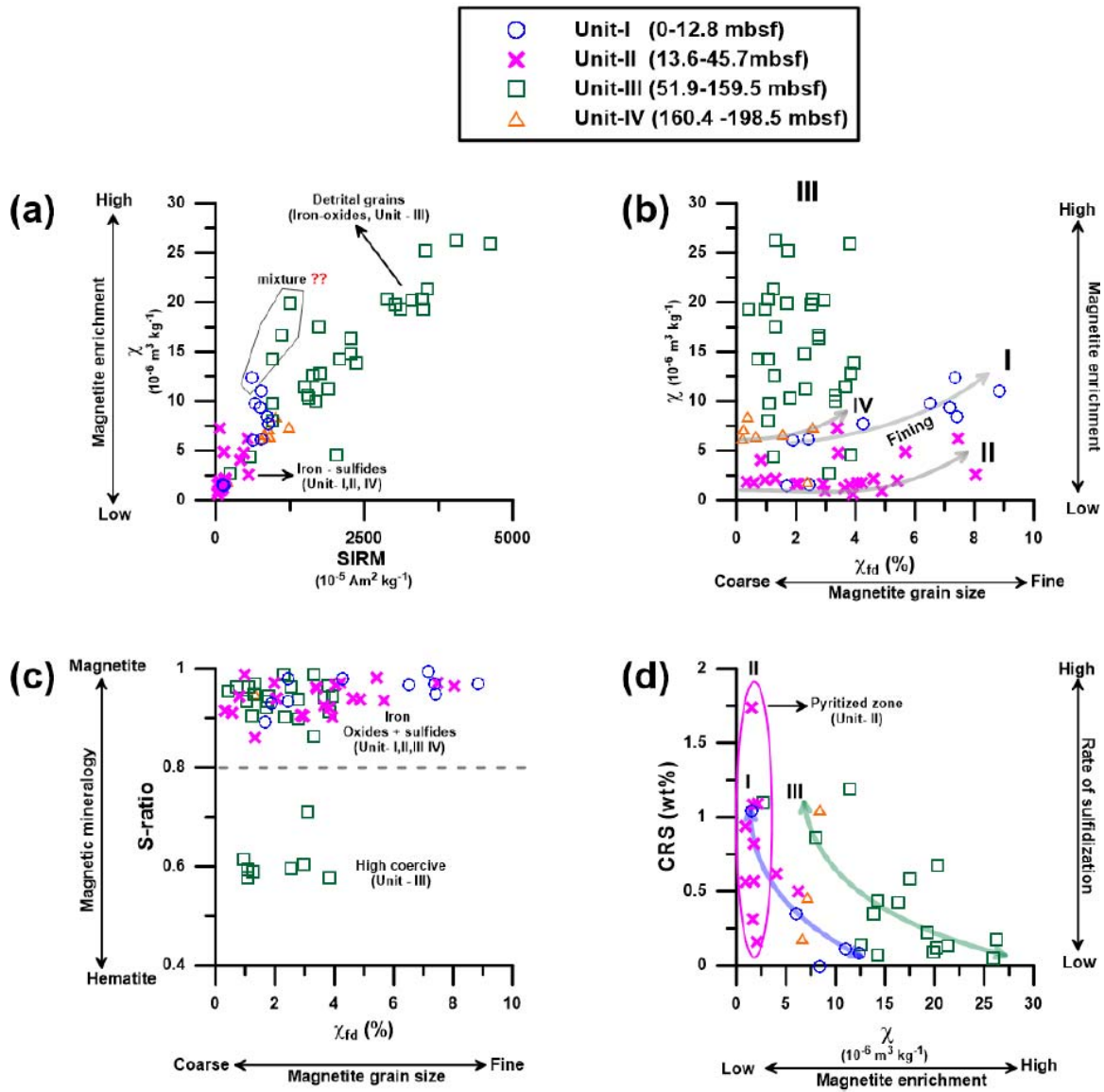


Figure 11

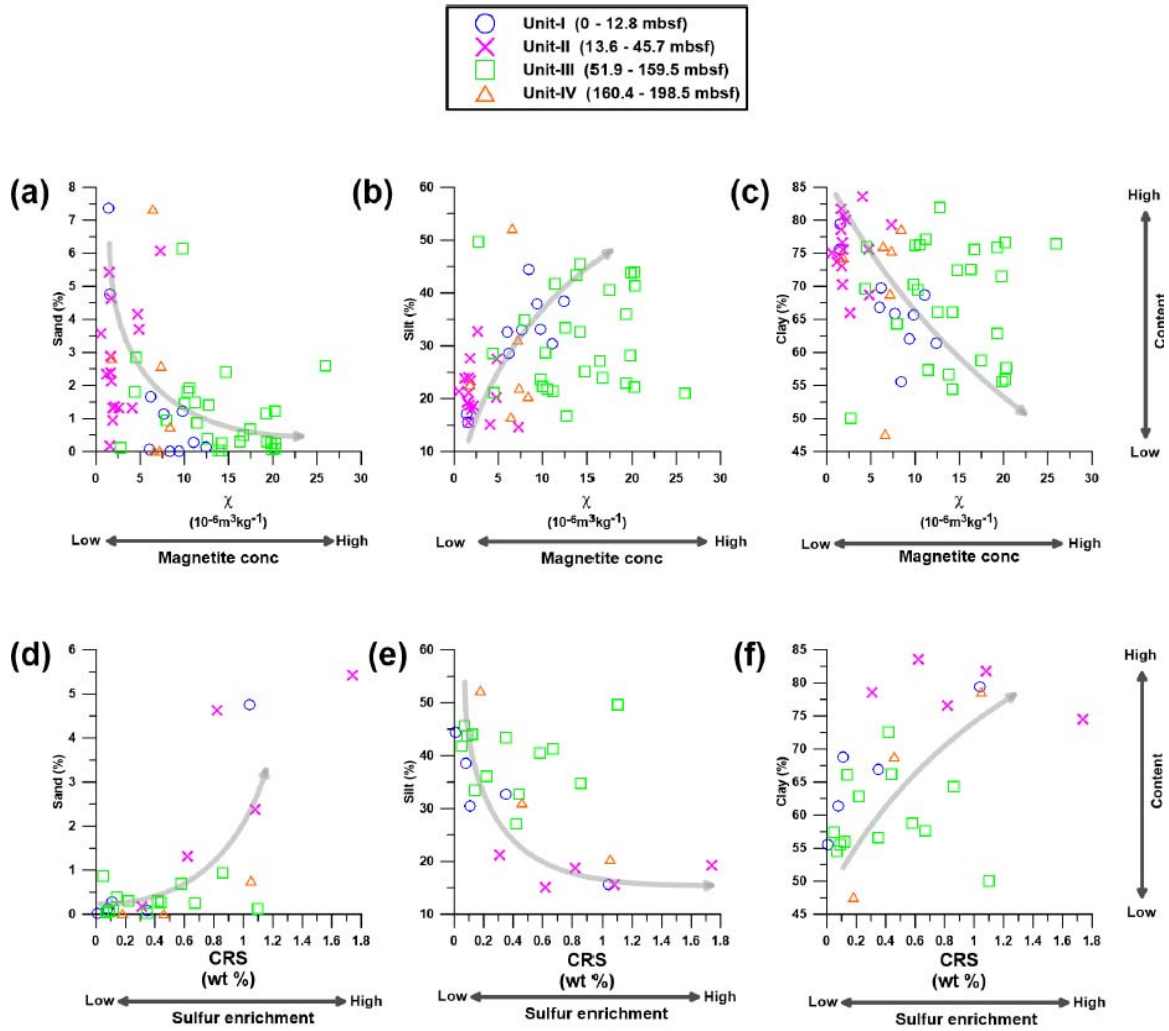


Figure 12

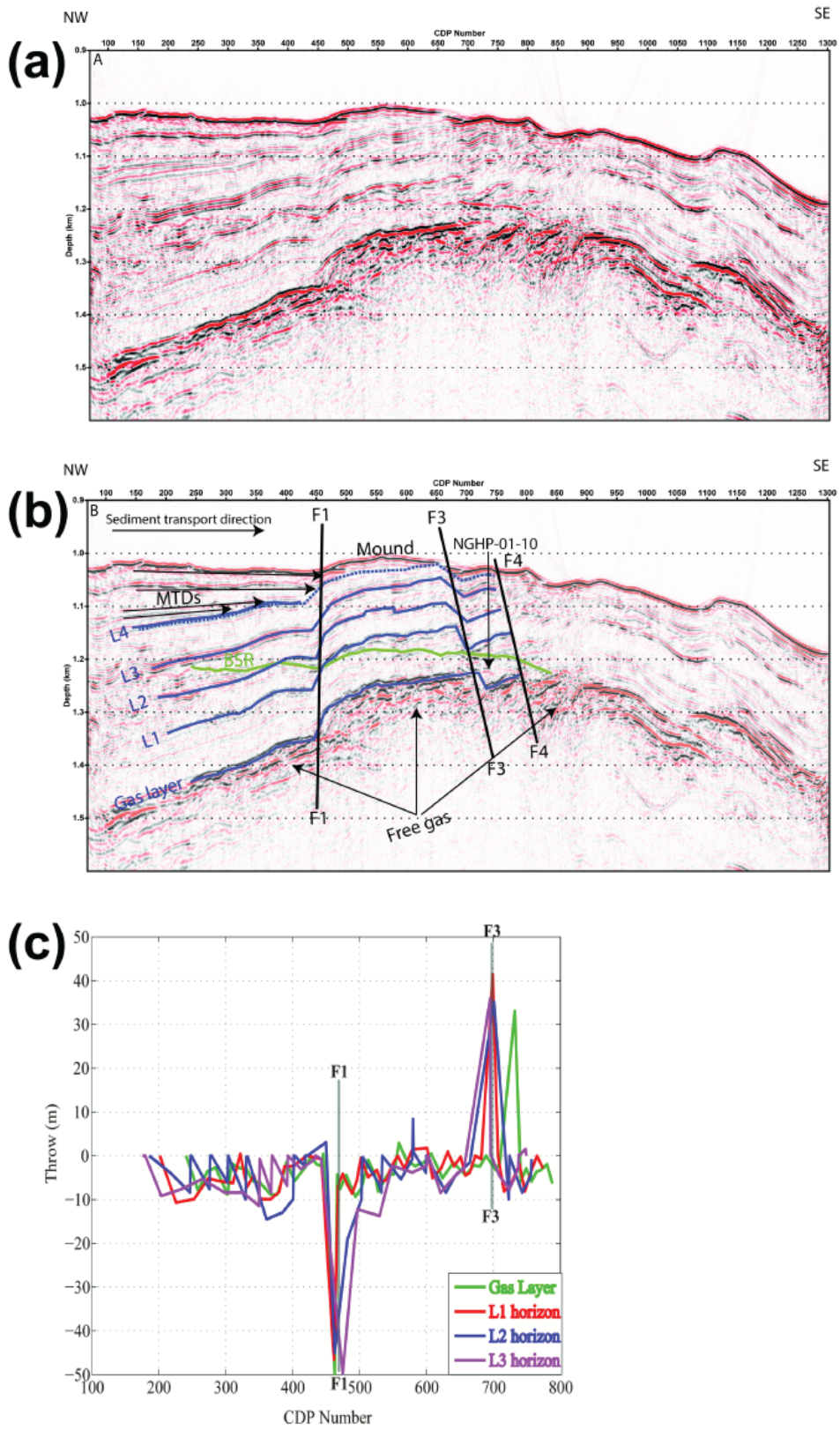


Figure 13

